MESOSCALE MODELING OF GRAIN REFINEMENT IN SOLIDS

A Thesis

by

MOHAMMED GOMAA EID FARAG ABDOELATEF

Submitted to the Office of Graduate and Professional Studies of
Texas A&M University
in partial fulfillment of the requirements for the degree of

MASTER OF SCIENCE

Chair of Committee,	Karim Ahmed
Committee Members,	Lin Shao
	Pavel V. Tsvetkov
	Bobak Mortazavi
Head of Department,	Michael Nastasi

December 2019

Major Subject: Nuclear Engineering

ABSTRACT

A phase field model was developed to simulate the grain refinement in solids. The model considers the interfacial energies of grain boundaries and bubble surfaces, strain energy associated with dislocations, and the chemical energy of gas atoms. This enables the model to simulate the formation and growth of sub-grains and bubbles in a self-consistent manner. The model results demonstrate strong effects of dislocation density (the magnitude and distribution), grain boundary energy, and bubble radius and number density on the formation of the sub-grains. For polycrystalline ceramic fuel UO_2 and the metallic fuel U-Mo, the model simulated the high burn-up structure (HBS) formation and evolution. In the case of UO_2, the model predicts the average size of the recrystallized grains within the range of 0.3 to 0.5 microns corresponding to a dislocation density range of $\rho = (2.5x10^{15} - 2.65x10^{15})\ m^{-2}$ or equivalently to 70 - 75 GWd/tHM burn-up. For the metallic fuel U-Mo, the HBS was determined to extend within a fission density range of $5.5x10^{21}\ fission/cm^3$ or equivalent to approximately 120 GWd/tHM. The corresponding U-Mo newly recrystallized average sub-grain size was concluded to be similar to the UO_2 case. These predictions agree with the reported data in the literature.

ACKNOWLEDGEMENTS

I would like to thank my committee chair, Prof. Karim Ahmed, and my committee members, Prof. Lin Shao, Prof. Pavel V. Tsvetkov, and Prof. Bobak Motazavi, for their guidance and support throughout the course of this research.

Thanks also go to my friends and colleagues and the department faculty and staff for making my time at Texas A&M University a great experience.

Finally, thanks to my parents and siblings for their encouragement and to my wife, Taghred Essa and children (Khaled, Lareen, and Murad) for their patience and love.

CONTRIBUTORS AND FUNDING SOURCES

This work was supervised by a thesis committee consisting of Professor Karim Ahmed [advisor] and Professors Lin Shao, Pavel V. Tsvetkov of the Department of Nuclear Engineering, Texas A&M University, and Professor Bobak Motazavi of the Department of Computer Science & Engineering, Texas A&M University.

The authors for this work would like to acknowledge the support from a faculty development grant from the Nuclear Regulatory Commission (NRC-HQ-84-16-G-0009). Portions of this research were conducted with the advanced computing resources provided by Texas A&M High Performance Research Computing.

NOMENCLATURE

HBS	High Burn-up Structure
MOX	Mixed Oxide Fuel
UO_2	Uranium dioxide
Al	Aluminum
U-Mo	Uranium Molybdenum
JMAK	Avrami Johnson Mahal Kinetics Model
SRX	Static Recrystallization
DRX	Dynamic Recrystallization
PSN	Particle Stimulate Nucleation
LWRs	Light Water Reactors
LEU	Low Enriched Uranium
RERTR	Reduced Enrichment and Test Reactors
MTR	Materials Test Reactors

TABLE OF CONTENTS

Page

LIST OF FIGURES

CHAPTER I

INTRODUCTION

1.1 Motivation and Objectives

All physical (e.g. thermal and mechanical) properties of polycrystalline solids such as yield stress, fracture strength, ductility, electrical breakdown strength, dielectric constant, etc. are strongly/highly influenced/affected by the underlying microstructure (grains size, morphology, and distribution) [1-4]. The grain boundaries have an important role in determining material properties [2, 5]. The finer grain sizes in the polycrystalline solids lead to a larger grain boundary area per unit volume, which alters the material microstructure and all the related physical properties. Furthermore, a larger grain size indicates a longer diffusion path for atoms and/or point defects before reaching the second-phase/grain boundaries and consequently leads to an impact on the material characteristics [1-2, 5-6].

The material behavior under extreme conditions, such as irradiation, high temperature, high stresses, etc., is strongly/highly dependent on the grain size [1-3, 5-7]. The grain boundaries serve as sinks for point defects and reduce the formation of undesirable microstructures such as voids and dislocation loops, which inversely influences the thermal and mechanical properties of the material [5-7]. Additionally, the fission gas swelling and release in irradiated uranium dioxide, UO_2 (the main ceramic nuclear fuel), and Uranium-Molybdenum, U-Mo (the metallic nuclear fuel), decreases with increasing grain size [8-13]. Therefore, examining the process of grain

refinement/recrystallization is important for all the industrial, academic, and technological applications.

At high burn-up values, the so-called high burn-up structure (HBS) develops in most of nuclear fuels [14]. The HBS displays a porous, fine-grained microstructure different than the as-fabricated large-grained microstructure. Originally, the HBS was described as the rim structure because of its confinement to the periphery (outer region) of the fuel pellet where there is higher burn-up and lower temperature conditions. However, in complex fuels such as Mixed Oxide (MOX), the HBS is not only restricted to the rim region, but it is allocated among high local burn-up locations (where Plutonium disposition causes more fission and more deformation) [14].

The driving force for HBS formation is the reduction of the strain energy by introducing defect-free new sub-grains at the expense of damaged/deformed grains [12-15].The reduction balances the increase of interfacial energy due to the production of new boundaries. The HBS formation is well known to highly influence the thermal and mechanical properties of nuclear fuels [12, 14-17]. Furthermore, HBS also determines the swelling and gas release rates, and therefore the overall fuel integrity and performance. The main proposed mechanisms of HBS are recrystallization and grain subdivision [10, 12, 14-16]. During the recrystallization process, new sub-grains nucleate and then grow until completely consuming the damaged grains. However, in the case of grain subdivision, the original large grains will divide into smaller sub-grains. Therefore, quantitative modeling of irradiation-induced recrystallization is a crucial need to enhance our understanding of the grain-refinement process in polycrystalline solids. By performing

such investigations, our insight will be improved, particularly regarding the HBS manner in nuclear fuel.

The main purpose of the current study is to model and simulate the process of the grain-refinement/recrystallization process and to utilize the model to investigate the HBS formation and evolution in UO_2 and U-Mo. We have utilized the phase-field (diffuse-interface) method, which is a robust modeling approach developed to study various phase transformations and microstructure evolution processes in heterogeneous materials [18]. The phase-field method has also been adopted to investigate irradiation consequences in nuclear materials [19-23] and to examine the irradiation-induced recrystallization [24-25]. In these models, the influences of fission rate and grain size on recrystallization kinetics were thoroughly investigated. However, the nucleation rate, newly sub-grains, and recrystallized grain morphology are assumed a priori based on classical nucleation theory. These assumptions restrict those models to predict only the kinetics of recrystallization. Furthermore, these hypotheses directly control the microstructure and overall kinetics. In order to alleviate the shortcomings of the above models, it is desirable to develop a general model which can relax those assumptions. Other modeling techniques, such as rate theory [26-27] and cluster dynamics [28-29], were utilized to study irradiation-induced recrystallization. While these techniques can predict the average recrystallization kinetics, they also manipulate the classical nucleation theory and neglect the heterogeneity of the underlying microstructure.

1.2 Contribution to Research

We present here a novel phase-field model for HBS formation and evolution. For simplicity, our model utilizes a continuum dislocation density field rather than resolving individual dislocations. Further, HBS formation is modeled as a phase transition. The self-arrangement of the dislocations into sub-grains could be employed in a process similar to the classical disorder-order transitions in alloys, with the characteristic that the dislocations, not the individual atoms, are undergoing self-organization. This model could simulate the grain growth process [30-31] by combining the stored strain energy contribution correlated to the formed dislocations under irradiation. Therefore, our model's main focus is where the nucleation of recrystallization is modeled explicitly without a priori assumptions on the nucleation rate and sites, or the size and morphology of the recrystallized grains.

The model generalization performs the capability to simulate the formation and the following growth of recrystallized grains. The consequences of the density and distribution/concentration of dislocations on the recrystallization kinetics were investigated in depth. The importance of gas bubbles (radius and number density) on the overall kinetics of HBS formation was also examined. Moreover, the model was evaluated by investigating simple test cases and various simulations were used to study the irradiation-induced recrystallization. We started by performing the growth rate modeling of a recrystallized grain and compared it with theoretical predictions, which was followed by an investigation of the particle-grain boundary interaction. Lastly, we presented a

quantitative analysis regarding the effect of various interface types (bubbles-matrix interfaces) on the recrystallization kinetics.

In conclusion, we produced a phase-field model to study and simulate the grain-refinement/recrystallization process in single/second-phase polycrystalline solids. The phase-field model relaxes nearly all the limiting assumptions manipulated in the classical and sharp-interface approaches. It could present an insight into the dynamics of the grain-refinement process, which influences the overall microstructure morphology and evolution and the thermal and mechanical properties of the material. By executing our model, we successfully captured the formation and evolution of HBS phenomena in nuclear fuel. The model results agreed well with published experimental investigations of HBS in UO_2 and U-Mo [8, 11, 13-14, 24-25, 32-34].

1.3 Thesis Layout

First, the technical background associated with the grain-refinement and recrystallization process is reviewed in Chapter II. In the first part of this chapter, the process of grain-refinement in solids (single and second-phases alloys) was discussed in detail. Additionally, a brief discussion related to solid-solid interfaces classification of crystalline systems according to the structure of the interfaces was conducted. The various models which were developed to study the irradiation-induced recrystallization, HBS formation and evolution processes, were summarized in several parts of this work. In the second part of Chapter II, the general concepts of the HBS formation and evolution in nuclear fuel are presented and discussed.

Chapter III introduces the development of the phase-field model to simulate irradiation-induced recrystallization and the HBS formation and evolution in polycrystalline nuclear fuel. First, the thermodynamic and kinetic formulations were introduced and the procedure to determine the model parameters was discussed. Lastly, we highlighted the numerical implementation details.

In Chapter IV, the results obtained by solving the phase-field model are presented and discussed. Test cases for benchmarking the model were conducted first. Then, quantitative investigations of the effects of dislocation/fission densities (magnitude and distribution), initial grain sizes, and the existence of second-phase particles (numbers and sizes) on the recrystallization kinetics in nuclear fuel (UO_2 and U-Mo) were executed. All the simulations performed in this study were conducted in 2D space due to computational cost limitations.

Finally, Chapter V summarizes the research conducted in this study and highlights the possible directions for future research. Parts of this thesis have been published in the Journal of The Minerals, Metals & Materials Society (JOM), DOI: 10.1007/s11837-019-03830-z.

CHAPTER II

TECHNICAL BACKGROUND

The main goal of this study is to investigate the process of grain refinement in porous solids using the phase-field approach. In the first section, the fundamentals of the refinement/recrystallization process are discussed. The formation and evolution of the so-called high burn-up structure (HBS) in nuclear fuels (UO_2 and U-Mo) are described and presented in the second section.

2.1 Grain refinement in solids

Grain refinement is considered as one of the most important phenomenas to material research approaches in the last few decades. Grain refinement enhances the formation of a fine equiaxed microstructure. Where the amount of new recrystallized grains increased, and might inhibit the growth of new grains especially under high deformation status (e.g. high dislocation density due to high irradiation effect). Generally, a finer grain size and second-phase particles (bubbles, pores, precipitates, etc.) limit the amount of dislocations and size of the grains, and provides a large influence on mechanical and thermal properties [1]. Though the grain refinement process was intensively studied for different alloys, there are more complications when studying the irradiation effects on nuclear materials. To have a better understanding of grain refinement, it is helpful to briefly describe the general annealing processes. Figure 1 illustrates the annealing process, which includes **recovery, recrystallization, and grain growth** [3, 35]. Generally, the dislocations initiated after cold-working or irradiating the material have a regular pattern due to the added energy

(e.g., heating). The new rearrangement leads to residual stresses initiation followed by an alleviated or relieved process of these stresses. The dislocation accumulation is the precursor of a new microstructure texture and results in a change of the thermal and mechanical properties [36]. In the **recovery process**, the releasing of point defects, vacancies, and their clusters starts to take place. Moreover, the process of dislocation annihilation or reorganization will be noticed in this process, inducing a significant change in the material structure and its mechanical properties [35].

After the recovery process, the Recrystallization process begins. **Recrystallization** is defined as ‘‘the formation of a new grain structure in a deformed material by the formation and migration of high angle grain boundaries driven by the stored energy of deformation” [4]. The main feature of the recrystallization phenomenon is the initiation of new non-deformed grains at the expense of the initially deformed grains. These new recrystallized grains were found to be unique in shape, size, and orientation. Moreover, it releases or eliminates the excess energy (due to deformation) from the materials [35]. Note that the Grain-refinement is a more general term than recrystallization and does not consider the driving force.

The recrystallization is more pronounced (generated faster) in the case of initially finer grains since, for a given deformation, the finer grains contribute more preferred nucleation sites. Concurrently, the recovery and sub-grain growth processes occur which leads to a reduction of the recrystallization driving force and a decrease in the recrystallization rate [3, 35].

The Grain Growth process can be described as the decrease in grain numbers and increase in the average grain size in a polycrystalline solid. Grain growth only occurs at sufficiently high temperatures. Due to the reduction in the total grain boundary area, the interfacial free energy decreases, which is the main driving force in the grain growth process. An alternative description of this process can be understood by considering the grain boundary movement. The atoms in this hypothesis are considered to diffuse less than the interatomic distance from both sides of the grain boundary, and therefore, the grain boundary will move in the opposite direction. Furthermore, the high-angle boundaries cause a replacement of deformed grains by newly formed deformation-free grains [35, 37].

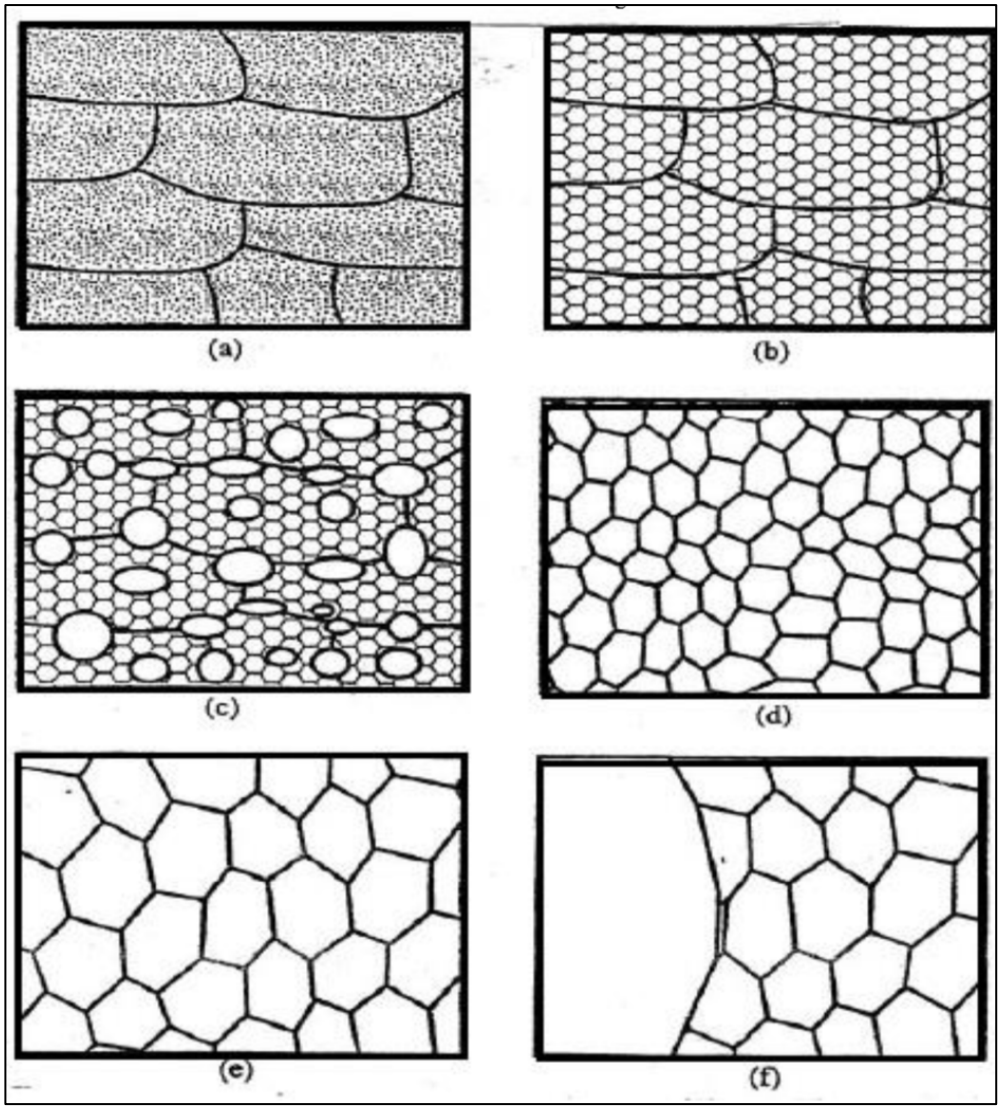

Figure 1 Schematic diagram for the main annealing processes: (a) deformed state, (b) Recovered (c) Partially recrystallized, (d) Fully recrystallized, (e) and (f) are the grain growth, reprinted from [3, 35].

2.1.1 Recrystallization of single-phase alloys

Recrystallization/grain refinement were investigated to understand the microstructure of the materials and treat the associated mechanical and thermal properties. This treatment mainly occurs through the release of deformation stresses. Early attempts of the recrystallization phenomenon performed analytical and empirical models to predict the recrystallization kinetics and microstructure [38]. In our investigation, a novel phase field model was constructed to describe the recrystallization evolution by predicting the recrystallization rate, critical temperature, critical deformation, and the final new sub-grain (deformation-free grains) size.

The recrystallization process can simply be considered as a thermally activated process consisting of two main sub-processes, nucleation and growth. The stored energy caused by the deformation (or dislocations density) is considered to be the main driving force for the recrystallization phenomenon [39-40]. Based on this description, the recrystallization initiation and evolution as well as a set of factors (not limited to this) affecting recrystallization will be presented in the following subsections.

2.1.1.1 Factors affecting the rate of recrystallization

While recent studies demonstrate recrystallization as a more complicated process, historically the factors affecting recrystallization kinetics were qualitatively established and presented as the laws of recrystallization [40]. The deformation (dislocation density) alters the stored energy and the number of preferred sites for the new sub-grains to be nucleated. A deformation threshold, or a minimum dislocation density, is essential to

provide the recrystallization driving force. The deformation density is also one of the main factors affecting the average size of the recrystallized grains, and the final grain texture. By increasing the dislocation density, the sub-grains per unit volume/area will increase, as well as finer grain sizes. The amount of dislocations/deformation is not the main cause of recrystallization, but the deformation orientation/distribution also has a large influence on the recrystallization rate. Additionally, the continuous heating after the recrystallization process leads to the grain growth, and therefore an increase in the final average grain size [39-40]. Figure 2 shows the effect of tensile strain on the aluminum recrystallization kinetics as an example of the recrystallization kinetics evolution. Finally, for better understanding of the recrystallization phenomena, a quantitative experimental and modeling analysis are required.

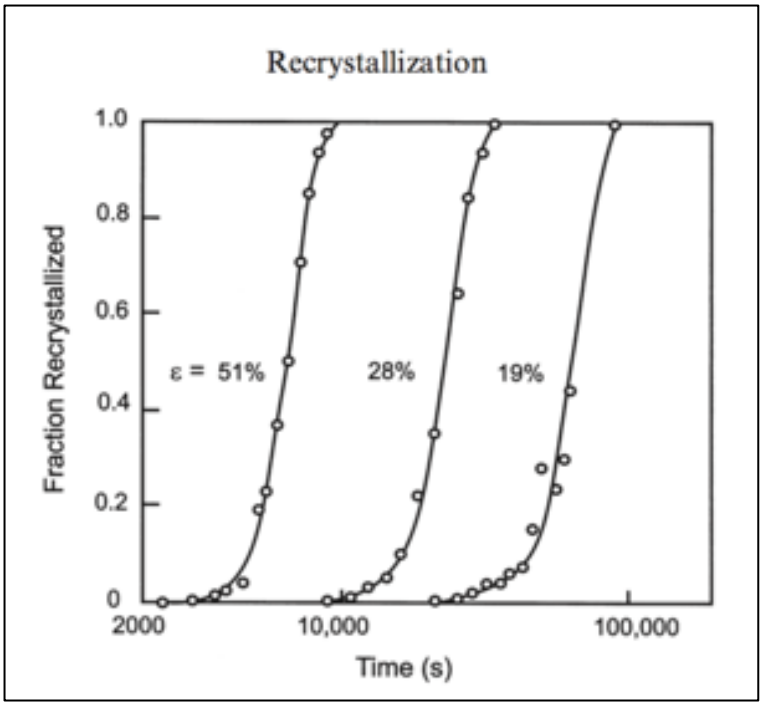

Figure 2 The effect of tensile strain on the recrystallization kinetics of aluminum annealed at 350 C, reprinted from [40].

2.1.1.2 The Recrystallization, nucleation and evolution

Recrystallization/phase transformations are usually characterized by developing the S-shaped or sigmoidal profile (see Figure 2). This unique shape can indicate recrystallization occurs at a slower rate at the beginning and end of the process, but faster in between. The initial slow rate is caused by the amount of time needed to create a significant number of new sub-grains (non-deformed grains). However, during the transitional period, the recrystallization kinetics are accelerated as the newly recrystallized grains grow and consume the old deformed grains. During this time, the new grains continue to form in the residual matrix (deformed grains). Once the recrystallization reaches completion, a few deformed grains remain and there are no significant sites for the new non-deformed grains to nucleate, leading to a slower rate of new grain production. The existing newly formed grains will start to touch one another, creating a larger number of boundaries, which hinders the growth rate.

Generally, the recrystallization process is a heterogeneous process, where the new deformation-free grains are nucleated and grow by the migration of high-angle grain boundaries at the expense of deformed grains. The recrystallization driving force is the release of the strain energy induced by the preceding process (e.g. Cold work or irradiation). The driving force, $-\Delta G_{\mathrm{recryst}}$, is given by [3]:

$$-\Delta G_{\mathrm{recryst}} = E_{\mathrm{elastic}} = \mathrm{C}\rho_{\mathrm{d}}\, G\, b^2 \qquad \text{(Eq. 2.1)}$$

where E_{elastic} is the elastic energy, C is a constant having a value between 0.5 and 1.0 [3], G is the material shear modulus, b is the burger vector, and ρ_{d} is the dislocation density,

which promotes the recrystallization this dislocation density could be as large as $5x10^{15}m^{-2}$ for highly deformed materials [3]. In addition, the recrystallized grains work effectively to reduce the stored energy in the matrix (specimen) [3]. The process of nucleation/recrystallization will take place only if the radius of the new grain (R) becomes larger than the value of critical radius (R_{crit}), which is expressed as follows:

$$R_{crit} = \frac{\alpha \gamma_{AB}}{P_D^{Rex} - P_Z} \quad \text{(Eq. 2.2)}$$

where, γ_{AB} is the boundary tension and α is a constant and is equal to 2 for spherical grains. Here, it should be pointed out that the recrystallization driving pressure (P_D^{Rex}) is the summation of Zener pressure (P_z) and the critical pressure (P_C) , i.e, ($P_D^{Rex} = P_Z + P_C$). In the case of particle-free materials or single-phase materials, no Zener pinning effect is considered ($P_Z = 0$), and $P_D^{Rex} = P_C$ (explained in detail in section 2.1.2.2.1). Accordingly, the recrystallization driving pressure (P_D^{Rex}) is considered as the additional pinning pressure from fine grains and requires an increased critical size for nucleation. These newly recrystallized grains are smaller than the initial deformed grains [40-41]. While these small grains can further grow and successfully become independent new grains. Generally, the recrystallization is formed by bulging out the high angle grain (with low dislocation density) into the higher stored energy grain, that leads to the new grain increase in size as the excess stored energy eliminated from the deformed one. This mechanism is conceptually treated as the random atomic fluctuations (classical nucleation theory) as with phase transformations [41].

2.1.1.2.1 The Classical and Generalized Johnson–Mehl–Avrami (JMAK) Model.

The sort of recrystallization process curve displayed in Figure 2 is a typical representation of various transformation reactions and can be explained in terms of the fundamental nucleation and growth processes. The pioneering research in this field was performed by Kolmogorov (1937), Johnson and Mehl (1939) and Avrami (1939), and is generally known as the JMAK model [42-43]. JMAK concluded nuclei/new grains are formed at a rate of ($\dot{N}$), and that grains grow into the deformed matrix at a linear rate of ($\dot{G}$). If the grains are supposed to be a spherical shape, then the volume changes as a function of (d^3), where d is the grain diameter. The fraction of recrystallized grains (X_V) increases rapidly with time at the beginning. However, the new grains will ultimately impinge on each other, consequently decreasing the rate of recrystallization, and eventually becoming zero when (X_V) approaches unity (a fully recrystallized domain) [40, 42-43]. This is also an alternative way to describe the famous recrystallization kinetics S-shape.

The amount of nuclei/grains (dN) which rise in a time period (dt) is smaller than ($\dot{N}dt$) because nuclei/grains cannot grow in the newly recrystallized sub-grains. The number of new sub-grains which appear in the recrystallized volume is $\dot{N}X_V dt$ and accordingly, the total number of grains (dN') which would have formed at a specific time including the recrystallized grains is expressed as $dN' = \dot{N}dt = dN + \dot{N}X_V dt$. If the volume of a recrystallizing grain is V at time t, then the substance/alloy recrystallization fraction would be represented as (X_{VEX}), which is the ratio between the recrystallized grain volume (or area for 2-D simulations) to the whole domain volume (or area for 2-D

simulations). If the incubation time (the time before the recrystallization to take place) is much shorter than t, then, the volume of recrystallized grains will be expressed as,

$$V = \frac{4\pi}{3}\dot{G}^3 t^3 \quad \text{(Eq.2.3)}$$

In the case of a constant rate of nucleation/recrystallization ($\dot{N}$ is constant), the recrystallization fraction will be formulated as $X_{VEX} = \frac{f\dot{N}\dot{G}^3 t^4}{4}$ [40]. For a small-time interval (dt), the volume increase will be described as dX_{VEX}. Since the materials unrecrystallized fraction is $1 - X_V$, then this expansion in volume can be represented as $dX_{VEX} = (1 - X_V)dX_{VEX}$, and the overall fraction of recrystallized material (X_V), can be written as

$$\boldsymbol{X_V = 1 - \exp\left(\frac{-\pi\dot{N}\dot{G}^3 t^n}{3}\right)} \quad \text{(Eq.2.4)}$$

This equation is usually denominated as the Avrami, Johnson–Mehl kinetics or **JMAK model** [40], where *n* is the Avrami Coefficient/Exponent and it varies based on various mechanisms of nucleation and growth. Avrami also investigated different scenarios when the nucleation rates were not constant. For example, ($n = 3$) for zero nucleation rate with interface-controlled growth and ($n > 2.5$) for small dimensions and increasing nucleation rate with diffusion-controlled growth [44].

The JMAK analysis is very simple to quantitatively model or investigate a process as complex as recrystallization. In particular, the variation in microstructure throughout recrystallization requires explanation from more parameters than Avrami parameters (X_V *or* X_{VEX}). However, the phase-field model (Diffuse-interface model - described in details in chapter III) provides further comprehensive simulations than possible by the

JMAK model. Furthermore, the phase-field can efficiently couple the thermal and mechanical aspects of the process for more reliable and feasible analyses [40, 45].

2.1.1.3 The recrystallized microstructure

The recrystallization process can generally be classified into two main categories known as static and dynamic recrystallization. Static recrystallization (SRX) refers to the recrystallization process during annealing. Dynamic recrystallization (DRX) describes the recrystallization which occurs during deformation at elevated temperatures. During recrystallization, material properties such as strength and hardness often change at much higher rates than during recovery [41]. During SRX, the size and energy advantage can be obtained by sub-grain growth or sub-grain coalescence. The initiation of recrystallization during SRX, denoted as incubation time, refers to the time needed to form large enough sub-grains that sufficiently surround the stored energy to overcome the forces caused by boundary curvature [41, 46]. However, for DRX, the critical dislocation density is often used in place of incubation time, and as explained previously, requires a threshold amount of dislocations to initiate the recrystallization process. Lastly, the magnitude of the initial grain size affects both the nucleation and growth processes. Factors such as a high strain or a small initial grain size result in a small final grain sizes, and hence faster recrystallization kinetics [40].

2.1.2 Recrystallization with second-phase particles

During recrystallization, a formation of a new type of non-deformed grain starts to take place; these new sub-grains are strain energy free grains. The second-phase particles play a significant role to hinder or enhance the deformation (dislocation) structure in terms of stored energy distribution and the preferred heterogeneous sites for recrystallization. In return, it should be recognized that deformation (especially in case of irradiation effects) may also lead to the evolution of second-phase particles. During either particle growth or dissolution, the interface boundary migration is likely to modify the particles shapes and deformation density. Additionally, second-phase particles interact with recrystallization by either retarding or accelerating nucleation, influencing the orientations of recrystallized grains or pinning their growth [41].

2.1.2.1 Particles Stimulated Nucleation (PSN) of recrystallization

It was observed that multiple nucleation of new grains occurs at large particles, which is shown in Figure 3. This observation was described as the well-known phenomena of Particle Stimulated Nucleation (PSN) which has been observed in many alloys [40]. In PSN, the preferred nucleation sites are well-defined regions around the larger second-phase particles (e.g. bubbles). In other words, the number of potential nuclei or formation of new grains can be defined, and therefore the recrystallized grain size can be controlled. Additionally, PSN will likely occur if the dislocation density is introduced below a critical temperature or more than the critical dislocation density (and a critical strain energy) [40].

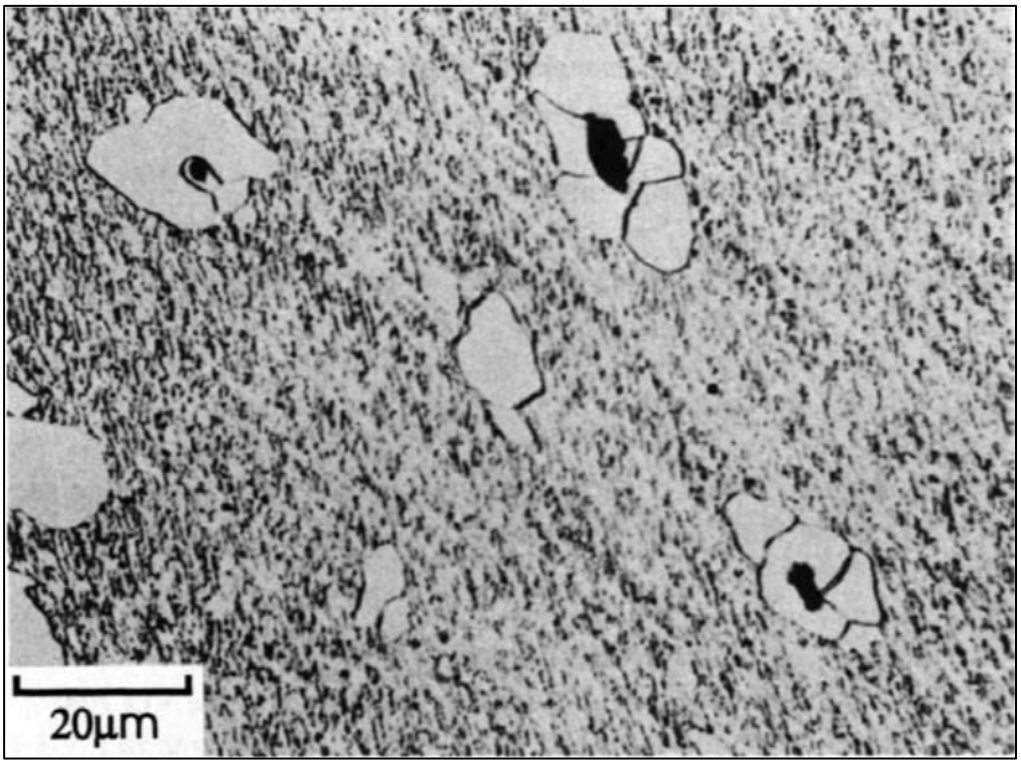

Figure 3 Particle stimulated nucleation of recrystallization at oxide inclusions in iron, reprinted from [40].

2.1.2.1.1 The influence of PSN on the recrystallization Microstructure

In second-phase particle alloys, larger particles tend to stimulate the recrystallization process. In composites with low particle-volume fractions, or compared to small particles, the coarse or larger particles are found to introduce a different impact on the final texture or microstructure. If recrystallization originates solely by PSN, it would be expected that the fully recrystallized microstructure would comprise equiaxed grains [40] of a size given by ($D \approx dF_V^{1/3}$), where D is the new recrystallized grain diameter, F_V is the volume fraction, and d is the particle diameter. The microstructures of the both deformed and fully recrystallized alloy (e.g. Al – 0.8% Si) are shown in Figure 4 [40]. In this figure, small grains were associated with the particles and formed by PSN; however, they exist as "island" grains within much larger grains. With more considerable dislocation density, more equiaxed grain microstructures will develop, with sizes corresponding to the particles' sizes and densities [40].

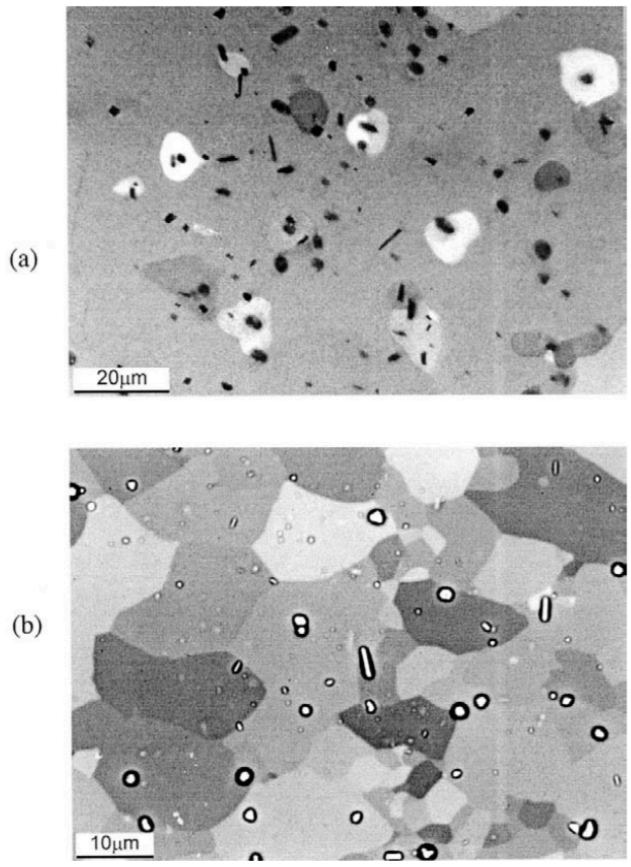

Figure 4 The recrystallized microstructures in a deformed and annealed crystal of Al–0.8%Si (a) PSN grains left as islands within rapidly growing grains (b) Equiaxed grains after larger strain, reprinted from [40].

2.1.2.2 Particle pinning during recrystallization

As the recrystallization is usually initiated via high-angle grain boundaries movement, therefore, the small particles/bubbles may inhibit nucleation/recrystallization. Generally, the fine particles limit the average sub-grains size; and the recrystallization will be suppressed if these particles are small enough to prevent the growth of sub-grains size to an extend such that a high-angle grain boundary can be formed. The gradients orientations tend to increase with increasing the dislocation densities, and therefore the

critical value to suppress the recrystallization - ($F_V^{1/3}/r$), where r is the particle/bubble radius - will also increase by increasing the dislocation densities [40].

2.1.2.2.1 Zener Pinning principle

Zener pinning [47] refers to the retarding force or pressure on the moving sub-grain boundaries by a dispersion of fine particles. As presented in figure 5 and by considering a moving flat boundary, three surface tensions are connected once the particle (C) reaches the boundaries (D) and (E), these surface tensions could be described as the boundary tension γ_{AB} and two particle surface tensions γ_{AC} and γ_{BC} (see figure 5) [41, 48]. The velocity of the boundary is then given by [49]:

$$v_b = M_b(F_b - N_p F_b) \quad \text{(Eq. 2.5a)}$$

where the subscript (b) denotes the boundary and (p) denotes the particle, v_b is the grain boundary velocity, M_b is the grain boundary intrinsic (particle-free) mobility, N_p is the number of particles per grain boundary area, and F_b is the pinning force that opposes the boundary pulling off the particle is given by Smith [47]:

$$F_b = 2\pi r cos\theta . \gamma_{AB} . sin\theta \quad \text{(Eq. 2.5b)}$$

As illustrated in figure 5, the region of $rcos\theta$ is the interface region between the particle and the grain boundary. By considering the pinning force to be only in Y-axis, hence the force in X-direction was set to be zero. Also, the maximum force F_{max} will be applied where $\theta = 45^{\circ}$, then,

$$F_{max} = \pi\gamma_{AB} \quad \text{(Eq. 2.6)}$$

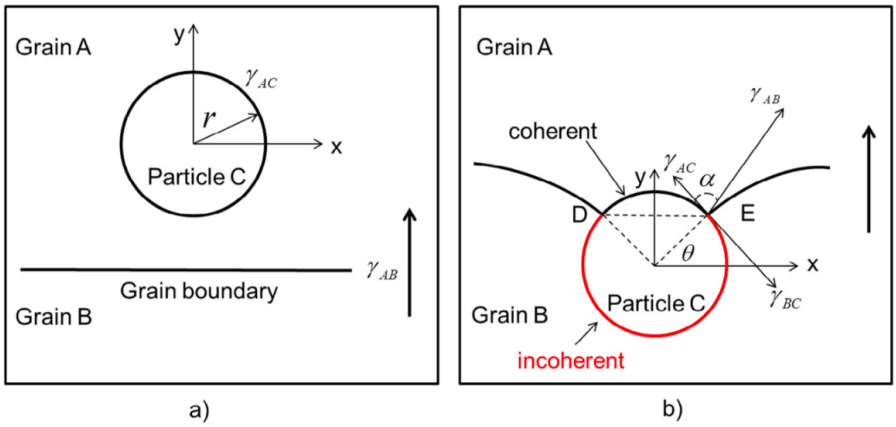

Figure 5 Schematic graph showing the interaction between a grain boundary and a spherical particle. (a) Before interaction; (b) During interaction, reprinted from [41, 48].

The total pinning force acting on the grain boundary could then be given by $(N_S.\pi r\gamma_{AB})$, where N_S is the surface density of the particles. If all the particles are assumed to act by the maximum pinning force on all of the boundaries, then the particles' surface density can be expressed as $N_V.r$, where N_V is the number of particles per unit volume. By assuming a spherical particle shape, then N_V can be expressed as $\frac{f_V}{\frac{4}{3}\pi r^3}$, where f_V is the particle volume fraction [41]. This yields the classical Zener pressure expression $P_Z = \frac{3f_V\gamma_{AB}}{2r}$, and the boundary curvature expression $P_C = \frac{\alpha\gamma_{AB}}{R}$.

As expected, the growth process will be hindered/stopped if the Zener pressure (P_Z) value reaches the driving pressure due to the boundary curvature (P_C) since the grain size limitation status will be obtained. The limitation conditions for the grain size can be expresses as $D_{Lim} = \frac{4\alpha r}{3f_V}$ [41], where $\frac{1}{R}$ is the average curvature radius, and $\alpha = 2$ for spherical shape grains.

Another way to express the influence of Zener pinning is by defining the driving pressure ($P_D = \frac{\alpha \rho G b^2}{2}$) as offset by the Zener pinning pressure (P_z), and the critical particle (PSN) size to be $d_p = \frac{4\gamma_b}{\alpha \rho G b^2}$, where γ_b is the high angle boundary energy. Then grain growth becomes $d_g = \frac{4\gamma_b}{P_D - P_Z}$. Thus, as the Zener pinning force increases, the critical particle diameter for PSN increases. Finally, it can be concluded that the Zener pinning force/pressure can be considered to be one of the major factors to hinder/retard the recrystallization process. This can affect both the nucleation and the growth of the grains. It will also modify or change the recrystallization microstructure, and hence the thermal and mechanical properties of second-phase alloys in general [40].

2.1.2.3 The influence of second-phase particles and recrystallization on the mechanical properties

The second-phase particles' size, distribution, and volume fraction can be modified by thermomechanical processing, which helps in controlling the recrystallization microstructures along with several mechanical properties. By controlling recrystallization and the second-phase particles, the mechanical properties can be improved or deteriorated. Recrystallization is regularly followed by a decline in the strength and hardness of a material and a concurrent improvement in the ductility and elasticity.

2.1.2.3.1 Yield strength

Yield strength and tensile strength both can be strongly influenced by recrystallization microstructure and second-phase particles (size, distribution, etc.). A

common approach is consists of linearly adding different contributions to the yield stress (σ_y) can be expressed as $\sigma_y = \sigma_0 + \sigma_{ss} + \sigma_{GB} + \sigma_\rho + \sigma_P$ [41], where σ_0 is a material constant related to the lattice resistance to the dislocation motion, σ_{ss} is the stress due to the solid solution, σ_{GB} is stress caused by the grain boundaries, σ_ρ is the stress by the dislocation densities, and σ_P is stress from particles existence [41, 50]. For the alloys systems with non-deformable fine particles, the dislocations will bow around the particle during deformation under the Orowan stress (τ) with respect to particle spacing (2r). This is given by $\tau = \frac{Gb}{2r}$, where G and b are the shear modulus and Burgers vector respectively, and r is the particle radius [41].

If the fine particles deform by the influence of the dislocation density (or applied deformation), either due to their small sizes or low strength, they are then sheared by moving dislocations. This leads to a reduction in the strength of the particles by decreasing their sizes on the slip plane (see Figure 6.b), further leading to a preferred planar slip on a few slip planes (Figure 6.d), and eventually to the formation of shear bands [41, 51]. This change in dislocation density contributes to grain boundary strengthening. In conclusion, a significant contribution of the fine particles on the material strength was approved and justified [41, 52].

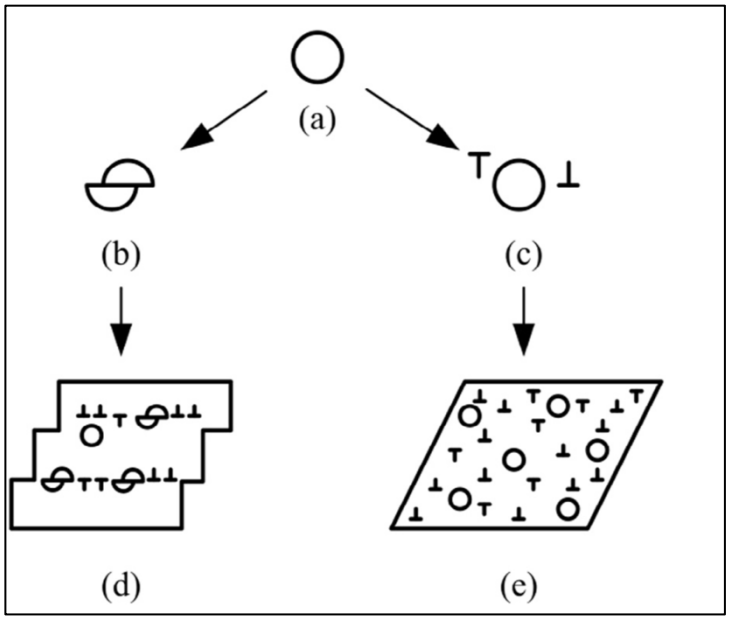

Figure 6 The effect of particle strength on the distribution of slip. A deformable particle (b) leads to slip concentration, as shown in (d). A non-deformable particle (c) results in more homogeneous slip, as can be seen in (e), reprinted from [40-41].

2.1.2.3.2 Ductility

Ductility is considered to be one of the most important material properties for the majority of materials and it is also often correlated to elongation and fracture properties. Ductile fracture incorporates failure by both cavitation and plastic instability. The requirements for high yield stress and good ductility are generally contradictory or competing each other. A large increase in ductility can be achieved if the void nucleation can be delayed or suppressed [41, 53].

Fractures can occur by plastic instability, such as the formation of shear bands in particle-free materials. In materials containing second-phase particles, fractures may appear prematurely due to void formation at these particles. A necessary condition for void nucleation is usually derived from energy considerations, i.e., the decrease in elastic

strain energy (e.g. resulting from the crack formation) be equal to or exceed the surface energy associated with the creation of a new surface: $\sigma = (\frac{2E\gamma_s}{\pi c})^{1/2}$ where E is the Young modulus, c is the particle size, and γ_s is the surface energy [41, 54]. This can explain why the materials with finer particles needs a larger stress to avoid the interfacial voids, and therefore improve ductility [41].

2.1.2.4 Types of Interfaces in solids

Many engineering properties of interest are determined by the structure of the solid-solid interfaces in the material [55]. Hence, a classification of solid-solid interfaces in crystalline systems according to the structure of the interface is required. Firstly, the free energy F of a system containing an interface of area A and free energy per unit area γ is given by ($F = f_0 + A\gamma$), where f_0 is the system initial free energy, here we assume all the system materials has the bulk properties. In addition to that, γ is the excess in free energy due to the interface effect. It also represents the work that must be done at constant pressure and temperature to create a unit area of interface. A crystalline solid-solid interface can be classified into three broad categories based on its structure, e.g., Coherent, Semi-coherent, and incoherent interfaces.

Coherent interfaces are described as interfaces where the lattice planes are continuous. Incoherent interfaces describe a structure in which there is discontinuity in lattice planes across the interfaces. The semi-coherent interfaces, which are the typical interfaces seen in engineering materials, are neither fully coherent nor incoherent, and are then essentially continuous lattice planes interspersed with regions of discontinuity. The following subsections will discuss the interfaces between different solid phases, i.e. where two adjoining crystals have different crystal structures and/or compositions. As described above, interface boundaries in solids can be divided into three classes: coherent, semi-coherent and incoherent.

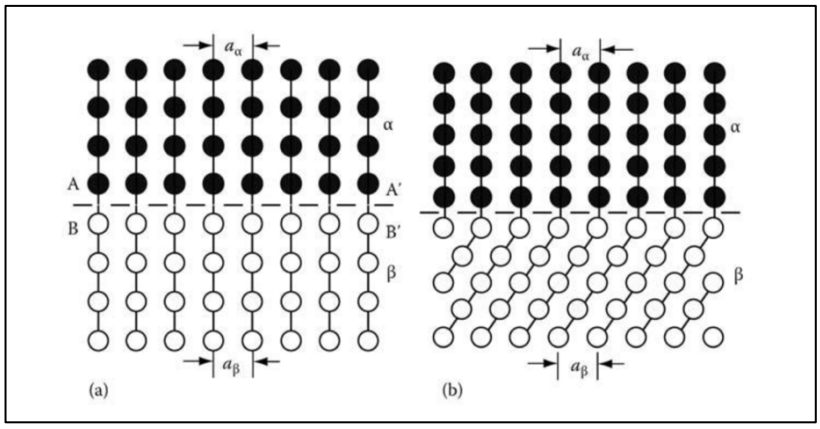

Figure 7 Coherent interfaces, (a) Crystals have different chemical composition with the same structure, (b) Having different lattices, reprinted from [55].

2.1.2.4.1 Fully Coherent Interfaces

A coherent interface is characterized by two crystals (two grains or particle-grain interfaces) with continuous lattice planes across their interface, so that the two different lattices will be existing on the same plane across the interface, as seen in figure 7. This can only be achieved if the interfacial plane has the same atomic configuration in both

phases, and further requires that the two crystals be oriented relative to each other. When the two crystals are joined along their close-packed planes with a parallel close-packed direction, the resultant interface is completely coherent (see figure 8). If the distance between the atoms at the interface is not identical, that leads to a change in the chemical contribution of the interfacial energy (γ_{ch}), but it is still possible to maintain coherency as presented in figure 9.

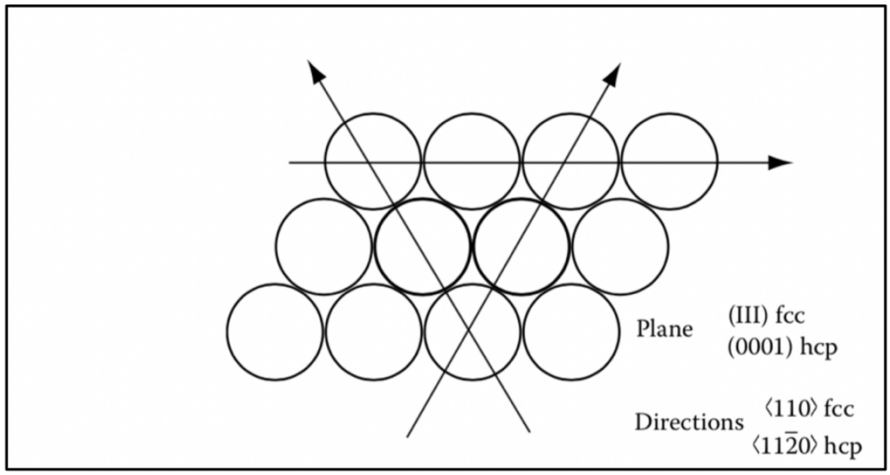

Figure 8 Close-packed plane and directions in fcc alloys, reprinted from [55].

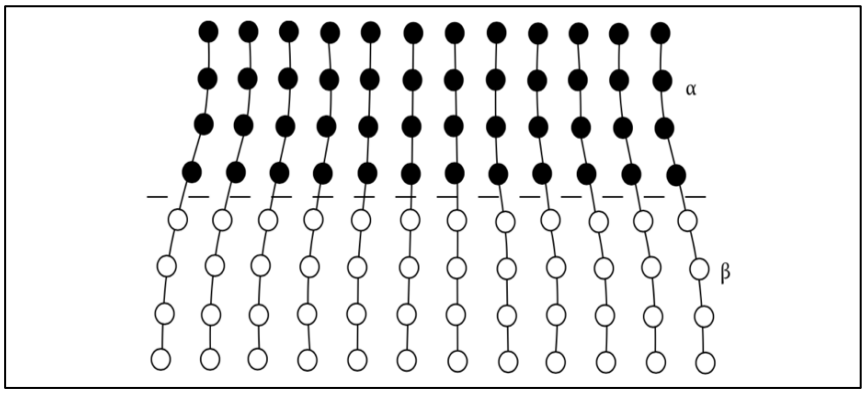

Figure 9 A coherent interface with slight mismatch leads to coherency strains in the adjoining lattices, reprinted from [55].

2.1.2.4.2 Semi-coherent Interfaces

The strains correlated among the coherent interface increase the total energy of the system, and hence the interfacial areas become energetically more favorable to replace a coherent interface with a semi-coherent interface (by introducing a large number of atoms misfits), as seen in figure 10. If $d\alpha$ and db are the stress-free interplanar spacings in the α and β phases respectively, the misfit δ between the two lattices (d) is defined by:

$$\delta = \frac{d_\beta - d_\alpha}{d_\alpha} \quad \text{(Eq. 2.7)}$$

If D is the distance between the dislocation (edge dislocations), then D can be expressed as $D = \frac{d_\beta}{\delta}$. If b is the Burger vector of dislocations and can be described as ($b = \frac{d_\alpha - d_\beta}{2}$). For small d , the edge dislocations with a spacing D are approximately given by $D \approx \frac{b}{\delta}$. This indicated a perfect matching except around the dislocation area, where the lattice planes found to be discontinuous. The semi-coherent interface energy can be approximated as the sum of two separate parameters: First, the chemical contribution γ_{ch}, like the case of fully coherent interface, and second is the structural term γ_{st}, which is the extra energy due to the structural distortions caused by the misfit dislocations, i.e. $\gamma_{(semi-coherent)} = \gamma_{ch} + \gamma_{st}$, where $\gamma_{st} \propto \delta$.

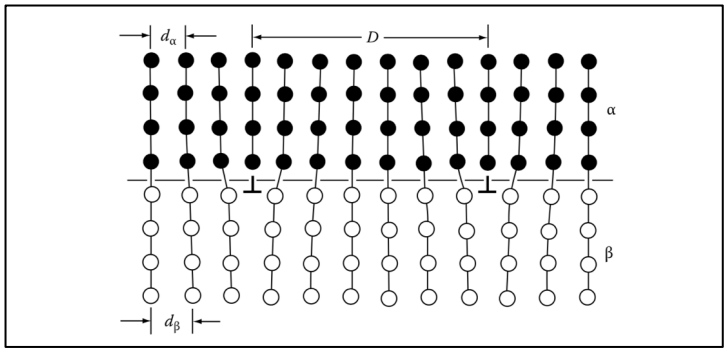

Figure 10 Semi-coherent interface, reprinted from [55].

2.1.2.4.3 Incoherent Interfaces

A perfect grain matching across an interface is nearly impossible when the two adjoining phases have very different atomic configurations. Often, the atomic pattern of the interatomic distances differs in the two faces, leading to an incoherent interface. In general, the incoherent interfaces are the result of two randomly oriented crystals joined across any interfacial plane, like as shown in figure 11. For simplicity, when the misfit parameter (δ) increase under the condition of $\delta > 0.25$, then the interface will be considered as incoherent interface. In other words, when dislocation existing at least at every four interplanar spacings, the region where the dislocation exist will have a poor fitting, results in an incoherent interface.

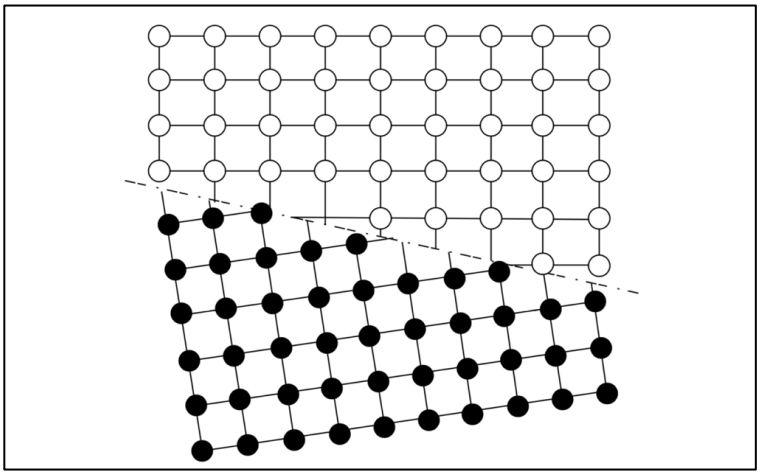

Figure 11 An incoherent interface, reprinted from [55].

2.2 The high burn-up structure (HBS) in nuclear fuel

For economic reasons and in anticipation of the operating conditions of next generation reactors, nuclear fuels have been continuously tested at high burn-up conditions. Most of these examinations have summarized the formation of high burn-up structure (HBS) [14]. The HBS incorporates finer grains textures along with porous particles which is different than the fresh fuel microstructure (large initial grains). The following sub-sections investigate the HBS formation and evolution in nuclear ceramic (UO_2) and metallic (U-Mo) fuel. Moreover, the mechanical and thermal properties associated with HBS were also discussed.

2.2.1 High burn-up structure in UO_2

Initially, the HBS was described as the rim structure due to its existence restriction to be at the outer region of the fuel, as observed in light water reactors (LWRs) [14]. Figures 12-13 are to present a micrograph of the HBS formation in UO_2 fuel [12]. As can be seen out of these figures, the HBS clearly forms at the rim region of the pellet. This is due to higher burn-up and lower temperature (less chances to anneal the dislocations) in this region.

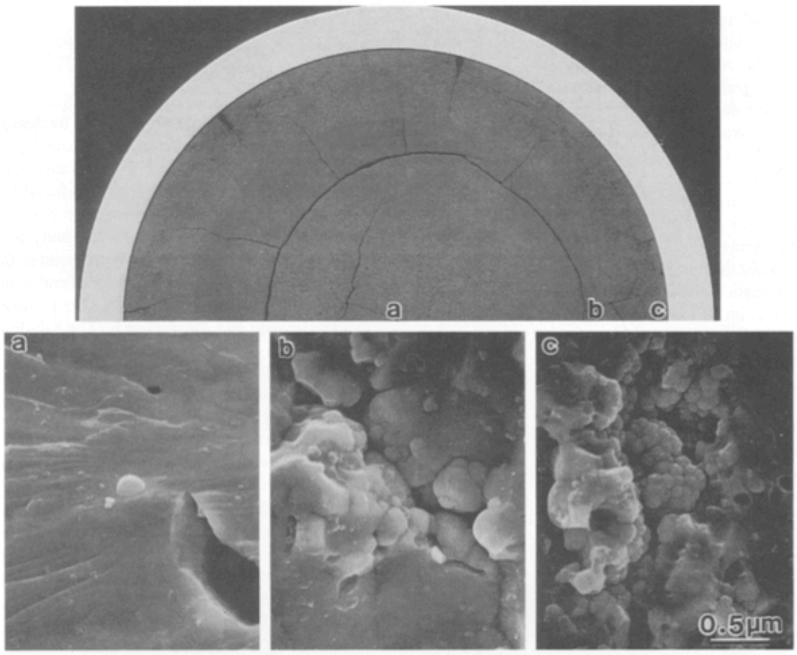

Figure 12 A micrograph of standard fuel pellet exhibiting the formation of high burn-up structure (HBS), reprinted from [12].

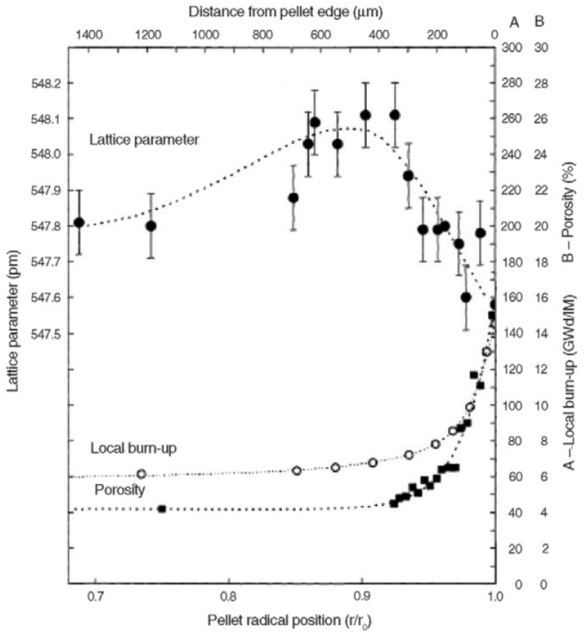

Figure 13 Variation of lattice parameter, porosity and local burn-up across the fuel pellet, reprinted from [14].

2.2.1.1 Formation of High burn-up structure in UO_2

HBS forms at the rim region of the UO_2 pellet due to higher burn-up (above 50 GWd/tHM [14]) and lower temperature (below 1373k [14]) in this region. The burn-up value at the periphery could be twice as large as in the pellet center as reported in Figure 13 [14]. This is created due to the occupation of higher Pu concentration emerging from the resonance absorption of epithermal neutrons by U^{238} [12, 14-15]. Nevertheless, in heterogeneous fuels such as MOX, the HBS is not only restricted to the rim region, but it is dispersed among high local burn up regions [14, 16]. HBS is observed in the colder regions of Mixed U-Pu oxide (MOX) fuel, where the Pu rich islands cause fission density and the corresponding local burn-up exceed the recrystallization threshold as can be seen in figure 14 [8]. HBS is associated with different operation conditions, but irradiation and temperature parameters were examined to have more impact on HBS formation and evolution.

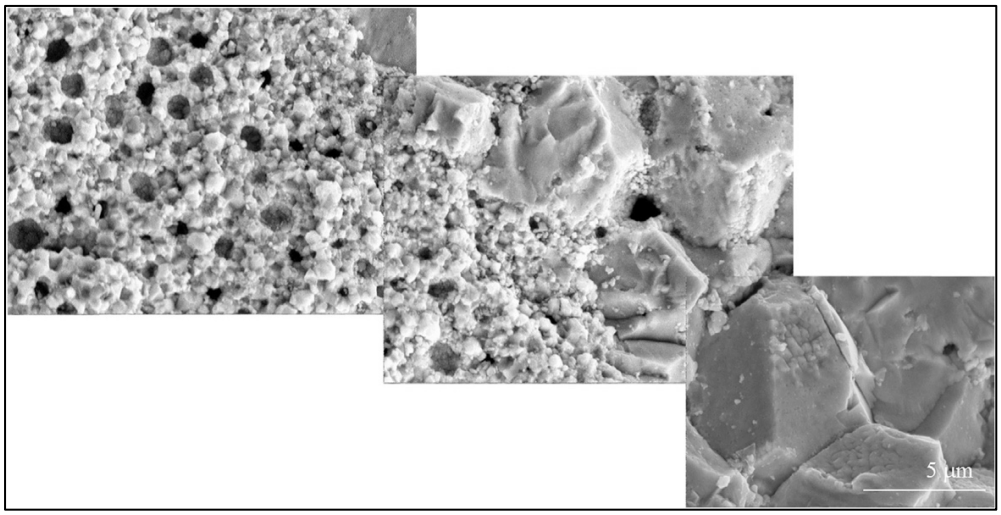

Figure 14 MOX fuel: Small sub-grains are observed in a fully restructured Pu-rich agglomerate while in the U-rich matrix restructuring is starting at the grain boundaries, reprinted from [8].

2.2.1.2 The driving force and different mechanisms for HBS in UO_2

Different terms were proposed to describe the HBS formation [10-12, 14-17]. The central proposed mechanisms are recrystallization and grain subdivision [10, 12, 14, 15-16]. In the recrystallization case, a new sub-grain nucleates and grows at the boundaries of the initially deformed grains. For the second case which is the grain subdivision, the original large grains will be divided into smaller sub-grains due to the higher dislocation densities.

Nonetheless, it is more difficult to describe the HBS for ceramic fuels such as UO_2 and MOX [16]. In this case, there is no general understanding of which mechanism is the subject to HBS development. Early studies were considering the HBS formation to be a subject of the recrystallization in UO_2 fuels [14]. This explanation was supported by the creation of sub-grains with high angle boundaries and on the surface of the bubbles as shown in Figure 15. Although, different investigations described a uniform formation of sub-grains (not just near to the bubbles or grain boundaries) with low angle boundaries, which is more related to the grain subdivision scenario [14].

Furthermore, more recent investigations described the formation of planar defects before the formation of HBS in UO_2 and MOX fuels [16]. Figure 16 illustrates the formation of certain planar defects in UO_2. It is considered that these planar defects are some sort of UO_2 over-structure with smaller lattice parameter [16]. It is estimated that the new sub-grains created at the surfaces of these planar defects that themselves ultimately converted into bubbles [16]. Finally, the specific behavior of these planar defects and the accurate aspects of their role in HBS formation are yet to be understood.

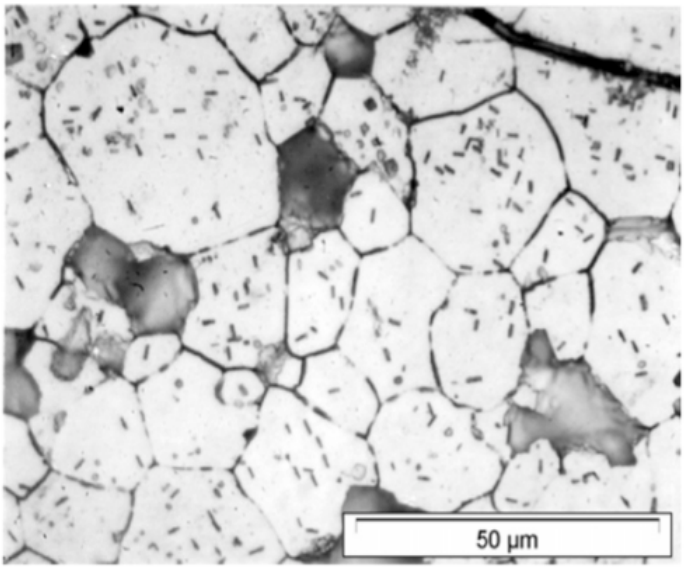

Figure 15 Formation of planar defects before the formation of HBS in UO_2, reprinted from [16]. The planar defects are believed to be some type of UO_2 over-structure with lower lattice parameter.

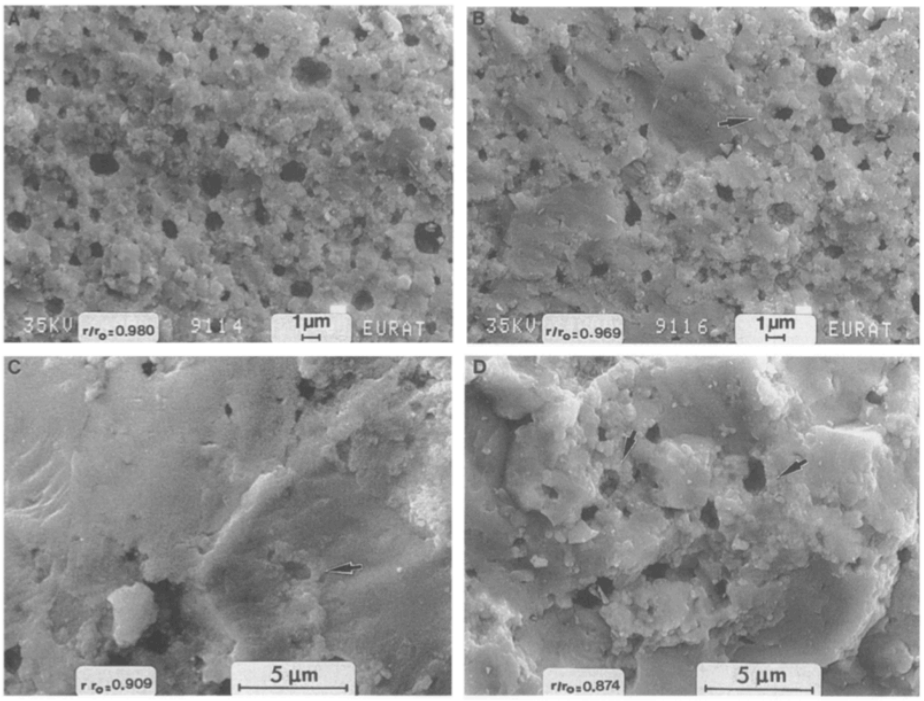

Figure 16 Formation of HBS in UO_2 fuel pellet, reprinted from [15]. Note that most sub-grains are formed close to both intra- and inter-granular bubbles, which was considered to be an evidence of recrystallization.

2.2.2 High burn-up structure in U-Mo

Uranium-molybdenum (U-Mo) composites have been widely investigated for power and test reactors extensively. A remarkable variation in the U-Mo fuel microstructure was observed when the fission density ($fission/cm^3$) exceeded a specific range ($(2.5\ to\ 3.5)x10^{21}\ f/cm^3$) [8]. The change in microstructure fairly follows the high burn-up structure (HBS) also known as "rim effect", as explained previously [8, 14, 16]. The structure is rising from grain refinement or recrystallization and when completely developed, it is identified by small grains ($\approx\ 0.2 - 0.3\ microns$) and a large number of intergranular pores [8].

In some circumstances, the mechanism of HBS formation is clear. For instance, in most metallic fuels, the recrystallization scenario seems more plausible. This is due to the fact that most of the newly formed grains in these systems are usually observed in the neighborhood of original grain boundaries and have high angle boundaries. This is captured in Figure 17 [56] that explains the recrystallization of new sub-grains in U-Mo metallic fuel. As obvious from the figure, the new sub-grains tend to develop closer to the grain boundaries of original grains and then dispersed into the bulk/matrix as the fission density rises. It is also clear from the figure that a threshold value for the fission density exists below which no HBS is recognized.

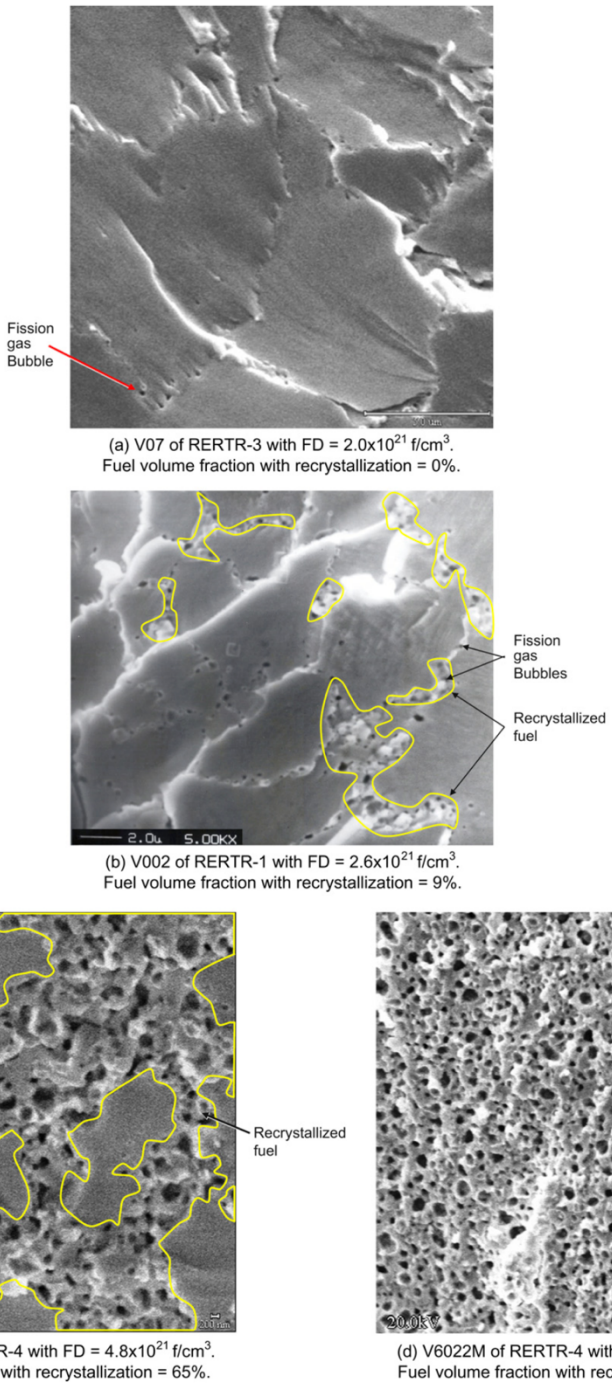

Figure 17 Development of high burn-up structure (HBS) in U-Mo at different fission density levels, reprinted from [56]. The recrystallization is believed to be the mechanism by which HBS forms.

Couple forms of U-Mo fuel have been produced and examined under irradiation influences. One is a monolithic fuel structure, in which a thin U-Mo alloy foil is placed between two planes of aluminum alloy cladding. The other is a dispersion fuel structure, expressed as U-Mo/Al, composed of U-Mo fuel particles that are dispersed in the Al matrix. The fueled region, including the U-Mo particles and Al matrix, is assigned to the fuel meat. Figure 18 represents the cross-sections of a monolithic fuel plate and a dispersion fuel plate [57].

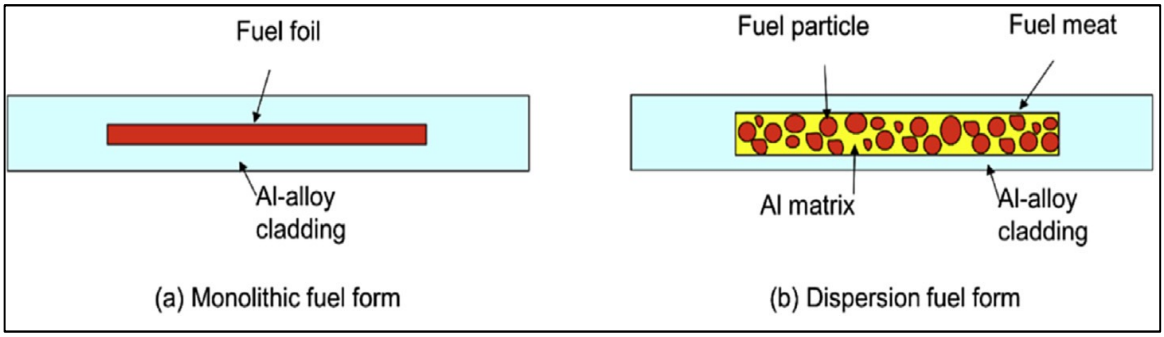

Figure 18 Schematic of the U-Mo fuel cross-section (as fabricated) (a) monolithic and (b) dispersion miniplates, reprinted from [57].

2.2.2.1 Types of Metallic Nuclear fuel (U-Mo)

2.2.2.1.1 Monolithic Fuel

Monolithic foil has the potential to obtain a fissile loading that would enable low Enriched Uranium (LEU) conversion of several reactors that cannot be converted with dispersions. The monolithic fuel type has some preferences over dispersion fuel: first, it has very high loading (up to 17.5 g U/cm^3 for U-7Mo) allowing more reactor conversions to LEU; second, it has a much lower surface area than dispersion fuel leading to fewer reaction with the aluminum plate and the central region of the plate [58].

2.2.2.1.2 Dispersion Fuel

U-Mo dispersion fuel, the elected fuel type by U.S. Reduced Enrichment and Test Reactor (RERTR), was admitted as an advanced fuel development in the last decades, but it has been found to show some restrictions under high temperature and burn-up circumstances. It is believed that in the normal operation conditions a non-preferable phase forms at the interface between the aluminum matrix and the fuel particles. By adding a few amounts of silicon to the matrix material, it may hinder the formation of the undesirable phase and enhance fuel irradiation performance under harsh operating conditions [58].

2.2.2.2 High burn-up structure of U-Mo dispersion fuel

In the last decade, various irradiations of Material Test Reactors (MTR) fuel plates consisting of low enriched U-7wt%Mo fuel dispersed in an Al matrix have been conducted under several conditions [8]. It was observed that the fuel swelling rate increases at fission density range of ($[2.5-3.5]x10^{21}f/cm^3$) [8]. The U-Mo fuel plate was studied and investigated extensively, consequently the fuel swelling was performed to be a function of location and local burn-up. This observation was demonstrated in many studies as one of the most significant concerns for U-Mo fuel type. Figure 19 is to show the swelling as a function of burn-up and position [8-9].

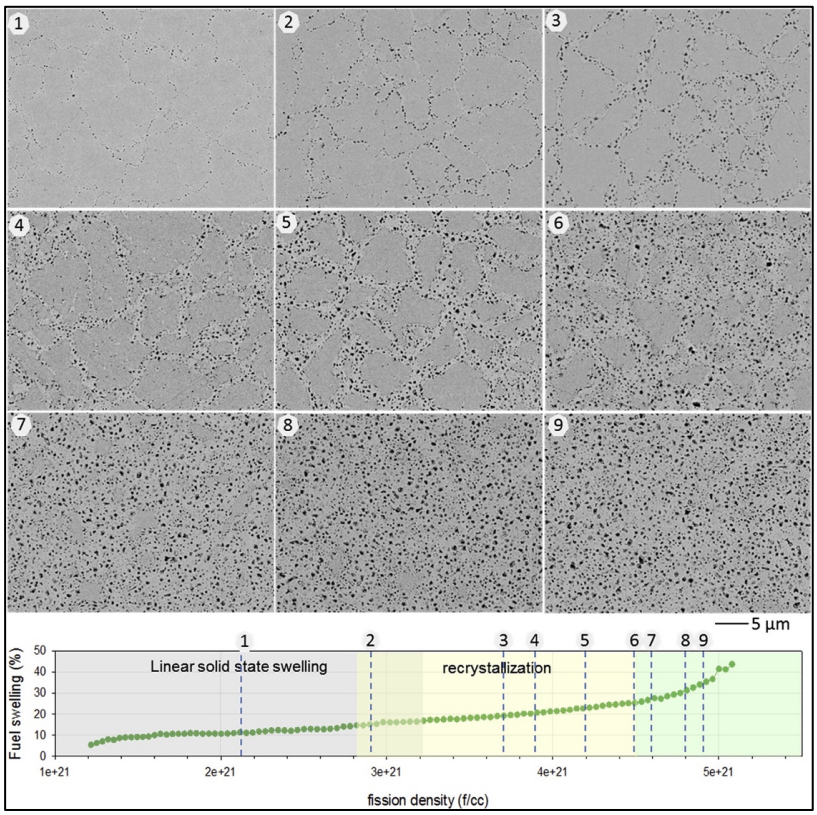

Figure 19 Evolution of the microstructure observed in samples from fuel plate U7MD1231 (ZrN coated U(Mo)), reprinted from [33] having a fission density as indicated in the graph, reprinted from [8].

For a fission density above a range of ($[2.5 - 3.5]\ x10^{21}\ f/cm^3$), a noticeable variation in the fuel microstructure is identified (as can be seen in figure 20). The change in U-Mo microstructure at this range of dislocation density, nearly resembles the high burn-up structure (HBS) [10, 14]. Similar to the UO_2 case, The HBS structure in U-Mo could be characterized by small grains (e.g., 200-300 nm) [8].

The lower temperature (no defects annealing) and the high damage in the lattice (Pu breeding and high fission density) both contribute to accumulation of stored energy in the lattice that drives recrystallization. This circumstance could be existing at typically operational burn-up (average ~50-60 GWd/tHM) [8]. Although, there are some extraordinary differences in the irradiation of ceramic (UO_2) and metallic UMo alloy fuels (e.g. temperature, enrichment, burn-up, etc.), there are a lot of similarities in the recrystallization process among these two fuel types [59]. It has been already reported the similarity of recrystallized grain structure after a burn-up of ~70 GWd/tHM in case of UO_2 and a fission density of $2.9\ x10^{21}\ f/\ cm^3$ for UMo fuel case [8, 60].

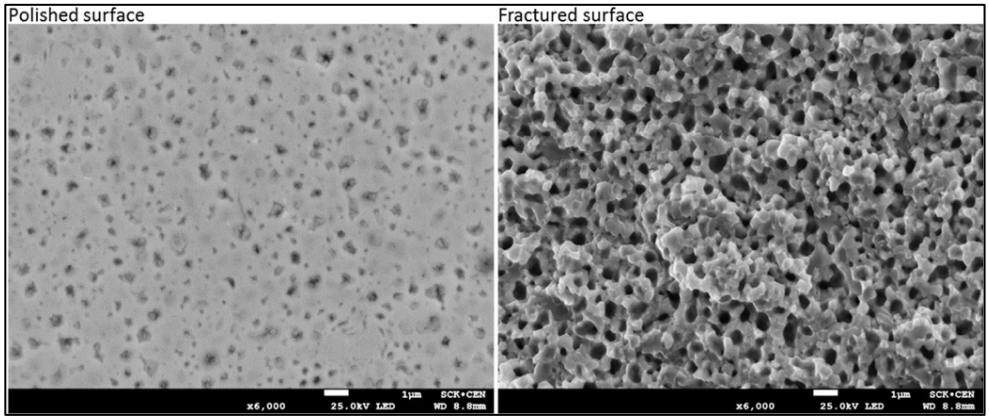

Figure 20 SEM image of the high burn-up sample in as polished and fractured surface condition, reprinted from [8].

CHAPTER III

PHASE FIELD MODEL DEVELOPMENT[1]

We treat HBS formation in UO_2 as a phase transition. The model developed here builds on the work by Moelans and others on grain growth, migration of recrystallization boundaries, and formulation of thermodynamically-consistent multi-phase-fields models [61-64]. The model is obtained through a transformation of the grand-potential model with a parabolic approximation of the chemical free energy as expressed in [64]. The resultant formulation is able to decouple the interfacial properties from bulk properties. This allows us to set the interface width independently from the bulk and interfacial thermodynamic properties and hence facilitates simulating larger domains at a lower computational cost [64]. The formation of new grains is directly accounted for by adding the strain energy contribution to the free energy and stochastic terms to the kinetic evolution equations.

The main goal, is to model and simulate the process of HBS formation and evolution in UO_2 and U-Mo. To that end, we utilize the phase-field method, which is a powerful modeling approach that has been used to investigate different types of phase transformations and microstructure evolution processes in heterogeneous materials [18]. The phase-field method has also been adapted to investigate irradiation effects in nuclear materials [19-23]. The phase-field modeling approach has recently been employed to investigate the irradiation-induced recrystallization [24-25]. In these studies, the effects of

---

[1] Reprinted with permission from Springer "Mesoscale Modeling of High Burn-Up Structure Formation and Evolution in UO2" by M. Gomaa Abdoelatef, Fergany Badry, Daniel Schwen, Cody Permann, Yongfeng Zhang, and Karim Ahmed, 2019. JOM, Copyright [2019] by The Minerals, Metals & Materials Society (JOM).

fission rate and grain size on recrystallization kinetics were thoroughly investigated. However, in those models, the nucleation rate, recrystallized grain size, and recrystallized grain shape/morphology are assumed a priori based on classical nucleation theory. This limits those models to predict only the kinetics of recrystallization. Moreover, those assumptions directly control both the resultant microstructure and the overall kinetics. Therefore, establishing a general model that relaxes these assumptions is desirable.

We introduce here a novel phase-field model for HBS formation and evolution. For simplicity, our model utilizes a continuum dislocation density field instead of resolving individual dislocations. Moreover, HBS formation is modeled here as a phase transition. Particularly, the self-arrangement of the dislocations into sub-grains can be treated in a way similar to the classical disorder-order transitions in alloys, with the distinction that the dislocations, not the individual atoms are the ones experiencing the self-organization. This model generalizes the grain growth models [30-31] by adding the stored strain energy contribution associated with dislocations formed under irradiation. Such generalization makes this model capable of simulating the formation and subsequent growth of recrystallized grains. The effects of the density and distribution of dislocations on the recrystallization kinetics were thoroughly investigated. Moreover, the influence of gas bubbles on the overall kinetics of HBS formation was also examined.

3.1 Phase Field Modeling of irradiation-induced recrystallization

Here, we use several order parameters to fully describe a typical HBS microstructure as depicted in Figure 21. In order to achieve that goal, such a set of phase fields order parameters must be able to distinguish between three different microstructural features, e.g., deformed grains, recrystallized grains, and bubbles. We use ρ for the dislocation density where $\rho \neq 0$ in a deformed/damaged grain and $\rho = 0$ in a recrystallized grain and inside the bubbles. c is the gas site fraction and $\tilde{c}$ is the normalized gas concentration. The normalized concentration is defined as $\tilde{c} = \frac{c-c^{eq}}{1-c^{eq}}$, such that it equals 0 in the solid and 1 in the bubble. c^{eq} is the equilibrium gas concentration in the matrix. In the following, for simplifying we will drop the tilde ($\sim$) when we refer to $\tilde{c}$ the normalized concentration. η_b uniquely identifies the bubble phase such that it equals to 1 inside the bubble and 0 everywhere else. The deformed/damaged matrix grains are represented by a set of non-conserved order parameters η_{dm_i}, while the recrystallized matrix grains are represented by another set η_{rm_i}.

Following the theory of gradient thermodynamics suitable for heterogeneous systems [23], the total free energy of the system is assumed here to have the form

$$F = \int f_{int} + f_b^{Th} dV \qquad \text{(Eq. 3.1)}$$

In the above Eq., f_b^{Th} is the bulk thermodynamic free energy, while f_{int} represents the interfacial free energy due to bubble (free) surfaces and grain boundaries. The interfacial free energy is given by

$$f_{int} = A\begin{bmatrix} 0.25 + 0.25\left(\sum_i \eta_{dm_i}^4 + \sum_i \eta_{rm_i}^4 + \eta_b^4\right) - 0.5\left(\sum_i \eta_{dm_i}^2 + \sum_i \eta_{rm_i}^2 + \eta_b^2\right) \\ +\gamma_{dm}\sum_i \sum_{j>i} \eta_{dm_j}^2 \eta_{dm_i}^2 + \gamma_{rm}\sum_i \sum_{j>i} \eta_{rm_j}^2 \eta_{rm_i}^2 \\ +\gamma_{rdm}\sum_i \sum_j \eta_{rm_j}^2 \eta_{rm_i}^2 + \gamma_b \eta_b^2\left(\sum_i \eta_{dm_i}^2 + \sum_i \eta_{rm_i}^2\right) \\ +\frac{k}{2}\left[\sum_i \left|\nabla \eta_{rm_i}\right|^2 + \sum_i \left|\nabla \eta_{dm_i}\right|^2 + |\nabla \eta_b|^2\right] \end{bmatrix} \quad \text{(Eq. 3.2)}$$

where A, γ_α and k are constants that determine the surface and grain boundary energies. This formulation assumes isotropic surface and grain boundary energies. Nonetheless, the model can be generalized for anisotropic cases in a straightforward manner as in regular grain growth models [31]. The thermodynamic bulk free energy is constructed as

$$f_b^{Th} = f^{ch} + f^{st} \quad \text{(Eq. 3.3)}$$

Here, f^{ch} is the chemical free energy and f^{st} is the stored strain energy associated with dislocations produced at high burn-up.

The strain energy of dislocations is expressed as

$$f^{st}\left(\rho, \eta_{dm_i}, \eta_{rm_i}, \eta_p\right) = \frac{1}{2} G b^2 \rho(r,t) h_{dm} \quad , h_{dm} = \frac{\sum_i \eta_{dm_i}^2}{\sum_i \eta_{dm_i}^2 + \sum_i \eta_{rm_i}^2 + \eta_b^2} \quad \text{(Eq. 3.4)}$$

where G is the shear modulus and b is the length of the Burgers vector. h_{dm} represents the fraction of deformed matrix grains in the domain. The effective/average dislocation density can then be calculated as,

$$\rho_{eff} = \frac{1}{V}\int \rho(r,t) h_{dm}(r,t) dV \quad \text{(Eq. 3.5)}$$

The dislocation density $\rho(r,t)$ can vary with space and time. In most simulations here, for simplicity, $\rho(r,t)$ was taken as a constant for all the damaged grains. However, we also investigate the effect of non-uniform dislocation density.A parabolic approximation of the chemical free energy of the bulk phases is used here, namely,

$$f^{ch} = B(c - h_b)^2 \text{ , } h_b = \frac{\eta_b^2}{\sum_i \eta_{dm_i}^2 + \sum_i \eta_{rm_i}^2 + \eta_b^2} \quad \text{(Eq. 3.6)}$$

where B is a constant that sets the value of the chemical free energy and h_b represents the bubble fraction. This specific form eliminates any contribution of the chemical free energy to the interfacial energy as demonstrated in [64]. Note that this form assumes equal curvatures of the parabolas representing the matrix and bubble phases. This is acceptable if one assumes the bubbles have their equilibrium pressure, and hence the value of the sole curvature can be used to represent the excess free energy in the matrix due to gas atoms supersaturation. Specifically, we fix the parabola such that the chemical potential calculated from (Eq.3.6) approximates the exact chemical potential given by the ideal solution form, e.g.,

$$2B\overline{c} = \frac{K_B T}{\Omega} ln \frac{\overline{c}}{c^{eq}} \quad \text{(Eq. 3.7)}$$

Here, K_B is Boltzmann constant, Ω is the atomic volume, T is the absolute temperature, $\overline{c}$ is the average gas concentration in the matrix, and c^{eq} is the equilibrium gas concentration in the matrix. The equilibrium gas concentration has a regular form, viz.,

$$c^{eq} = \exp\left(-E^f / K_B T\right) \quad \text{(Eq. 3.8)}$$

where, E^f is the solution energy of a gas atom.

The evolution equations for the phase fields/order parameters can be derived from the principles of irreversible thermodynamics [23]. The non-conserved order parameters evolve according to Allen-Cahn Eqs. [63] as

$$\frac{\partial \eta_b}{\partial t} = -L_b \frac{\delta F}{\delta \eta_b} = -L_b \left(\frac{\partial f^{int}}{\partial \eta_b} + \frac{\partial f^{ch}}{\partial \eta_b} + \frac{\partial f^{st}}{\partial \eta_b} - k\nabla^2 \eta_b \right) + \xi_b \ , \qquad \text{(Eq. 3.9.a)}$$

$$\frac{\partial \eta_{dm_i}}{\partial t} = -L_{dm_i} \frac{\delta F}{\delta \eta_{dm_i}} = -L_{dm_i} \left(\frac{\partial f^{int}}{\partial \eta_{dm_i}} + \frac{\partial f^{ch}}{\partial \eta_{dm_i}} + \frac{\partial f^{st}}{\partial \eta_{dm_i}} - k\nabla^2 \eta_{dm_i} \right) + \xi_{dm_i} \quad \forall i \qquad \text{(Eq. 3.9.b)}$$

$$\frac{\partial \eta_{rm_i}}{\partial t} = -L_{rm_i} \frac{\delta F}{\delta \eta_{rm_i}} = -L_{rm_i} \left(\frac{\partial f^{int}}{\partial \eta_{rm_i}} + \frac{\partial f^{ch}}{\partial \eta_{rm_i}} + \frac{\partial f^{st}}{\partial \eta_{rm_i}} - k\nabla^2 \eta_{rm_i} \right) + \xi_{rm_i} \quad \forall i \qquad \text{(Eq. 3.9.c)}$$

Here, L_b is a constant related to the bubble surface mobility, L_{dm_i} is a constant related to the boundary mobility of a deformed/damaged matrix grain, L_{rm_i} is a constant related to the boundary mobility of a recrystallized matrix grain, and ξ_α are stochastic terms that facilitate nucleation of grains or bubbles. In contrast to Langevin Eq., the stochastic terms here not only represent the thermal fluctuations of atoms/particles, but they also account for the cutoff of any fast degrees of freedom necessary for deriving coarse-grained free energy. Adding those terms to the evolution equations. enables them to explore other evolution paths in the vicinity of the most probable path in the phase space. Using constant mobility coefficients is equivalent to the assumption of isotropic grain boundary and bubble surface mobilities. Nevertheless, the extension to the anisotropic case can be achieved by following the standard approach used before in the models of solidification and grain growth [23, 30-31].

The gas atom concentration is governed by a Cahn-Hilliard type diffusion Eq., e.g.,

$$\frac{\partial c}{\partial t} = \nabla \cdot (M \nabla \mu) + P + \xi_c \qquad \text{(Eq. 3.10.a)}$$

$$\mu = \frac{\delta F}{\delta c} = \frac{\partial f^{ch}}{\partial c} \qquad \text{(Eq. 3.10.b)}$$

In the above Eq., M is the chemical mobility of gas atoms, μ is their chemical potential, P is a source term representing the on-going production of gas atoms due to fission events, and ξ_c is a stochastic term similar to the ones discussed above. The chemical mobility is related to the diffusivity (D) through

$$\frac{\partial^2 f^{ch}}{\partial c^2} M = D \ , \qquad \text{(Eq. 3.11.a)}$$

$$2BM = D. \qquad \text{(Eq. 3.11.b)}$$

Using constant mobility here amounts to considering bulk diffusion to be the sole mechanism of gas atom diffusion. However, grain boundary and surface diffusion mechanisms can be added to the model as in the work of Ahmed. et. al. on grain growth in porous solids [65-66].

The effective dislocation density is prescribed according to a constitutive law. In general, the dislocation density can change with time and position. These dependencies represent the accumulation of radiation damage and the heterogeneity of damage expected in distinct types of fuels used in different reactor types. For the sake of simplicity, we utilize here an empirical relation that calculates the average dislocation density for a given burn-up (Bu), e.g., [11].

$$\log \rho_{eff} = 2.2x10^{-2} Bu + 13.8 \qquad \text{(Eq. 3.12)}$$

The deformed grains are assumed to have this dislocation density, while the recrystallized grains are dislocation free.

The phase field model parameters are directly related to the thermodynamic and kinetic parameters as follows [10, 64].

$$\gamma_{dm} = \gamma_{rm} = \gamma_{rd} = 1.5 \quad \text{(Eq. 3.13.a)}$$

$$\left(\frac{\gamma_b}{1.5}\right) = \left(\frac{\gamma_s}{\gamma_{gb}}\right)^2 \quad \text{(Eq. 3.13.b)}$$

$$A = \frac{3\gamma_{gb}}{4\ell} \quad \text{(Eq. 3.13.c)}$$

$$k = \frac{3}{4}\gamma_{gb}\ell \quad \text{(Eq. 3.13.d)}$$

$$L_{dm} = L_{rm} = \frac{4M_{gb}}{3\ell} \quad \text{(Eq. 3.13.e)}$$

$$L_b = 10\frac{D}{B\ell^2} \quad \text{(Eq. 3.13.f)}$$

In the above, ℓ is the diffuse interface width, γ_{gb} is the grain boundary energy, γ_s is the surface energy, and M_{gb} is the grain boundary mobility. As can be deduced from Eq. (3.13), it is assumed here that the recrystallized and deformed grains have the same boundary energy and mobility. However, this is not a model restriction, as clear from Eq. (3.13), but rather a simplification for the lack of data. (Eq.3.13.f) guarantees that the bubble surface motion is diffusion controlled. The grain boundary energy and surface energy of UO_2 are taken to be $1.04\,J/m^2$ and $1.8 \pm 0.3\,J/m^2$, respectively [67-68]. In case of U-Mo, the shear modulus, burger vector, surface energy of gas bubbles, grain boundary energy, and kinetic coefficient were taken as $36.0\,GP$, $3.42\,x\,10^{-10}\,m$,

$1.64\ j/m^2$, $0.36\ j/m^2$and $1.82x10^{-14}\frac{m^3}{j.s}$ respectively [24-25]. The grain boundary mobility of UO_2 is given by [69].

$$M_b = 9.21x10^{-9}\exp(-2.77ev/K_BT)\ m^4/(J.s) \quad \text{(Eq. 3.14)}$$

The shear modulus and the magnitude of the Burgers vector for UO_2 are taken as $G = 73\ Gpa$, $b = 0.39\ nm$ [11]. The interface width was set to $20\ nm$ in all conducted simulations (UO_2 and U-Mo cases). A temperature of $1200\ k$ is assumed for all the UO_2 simulations cases here.

3.2 Determination of model parameters and numerical implementation in MOOSE

The model was implemented using the open-source finite-element code MOOSE, which uses its built-in Grain Tracker algorithm [70] to reduce the computational cost. Grain Tracker is an algorithm implemented in MOOSE that allows using a few numbers of order parameters to represent a large number of grains, which facilitates performing large scale simulations of polycrystalline materials [70]. In 2D simulations, only 8 order parameters are required to represent a few thousand grains. The grain tracker algorithm was utilized here to handle both the deformed grains and the sub-grains (recrystallized grains). To that end, 8 more order parameters were reserved to represent the recrystallized grains (η_{rm_i}). They are initially zero, and once new grains are formed, they are given new identification numbers and represented by one of the reserved order parameters. Nucleation takes place directly due to the inclusion of the stochastic terms. A uniform random generator with zero mean was used for these stochastic terms. The magnitude of the stochastic terms was found not to affect the evolution appreciably, and it was set to 10^{-3} in all simulations. Lastly, the kinetic evolution equations were solved using the same

procedure summarized in [71]. Built-in MOOSE adaptive time and mesh steps were also utilized to speed up the simulations.

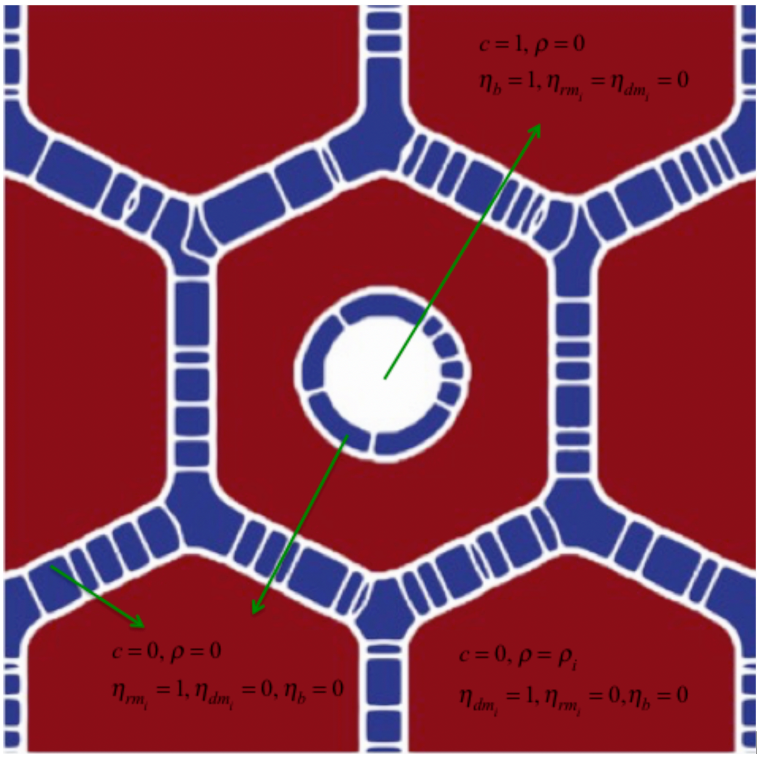

Figure 21 An illustration of the phase fields (order parameters) used to describe the HBS microstructure. Damaged grains are shown in red, recrystallized grains are shown in blue, and grain boundaries and bubbles are shown in white, reprinted from [74].

CHAPTER IV

RESULTS AND DISCUSSION

The results presented in this section were obtained by performing simulations of the phase field model for irradiation-induced recrystallization. In the first section, we conducted test cases to illustrate the capabilities of the model. Moreover, these test cases also serve as a benchmark for the model before simulating the real systems. In the second section, the model was utilized to study the irradiation-induced recrystallization (HBS formation) in UO_2 in case of presence/absence of gas bubbles. Finally, the last part of this result chapter was reserved for studying the HBS formation and evolution of dispersed U-Mo fuel by implementing our phase-field model.

4.1 Test Results

In this section, we examined the model by investigating simple test cases. In order to do that, we have carried out various 2D simulations to study the irradiation-induced recrystallization. First, we analyze the growth rate of a recrystallized grain and compare it with the theoretical predictions, tailgated by an examination of particle-grain boundary interaction investigations. Then, we investigate the irradiation-induced recrystallization (formation of the HBS). Finally, we presented a quantitative analysis regarding the influence of several interface classes (bubbles matrix interfaces) on the recrystallization kinetics.

4.1.1 The grain growth.

Before studying the irradiation-induced recrystallization, we analyze the growth of a recrystallized grain. This test case is crucial to provide a benchmark for our model. The velocity (v) of the grain boundary of the newly recrystallized grain (sub-grains), which grows at the expense of a deformed grain is given by

$$v = M_b(g - \gamma_b k) = \frac{3L\ell}{4}(g - \gamma_b k) \quad \text{(Eq.4.1)}$$

Where, g is the stored energy given by (Eq.3.4) and k is the curvature of the grain. Additionally, (Eq.3.13e) was giving an expression of the grain boundary velocity in terms of the phase field model parameters. Then, we introduced an investigation of the growth/shrinkage of a recrystallized grain (circle grain) inserted in a deformed matrix grain. Based on (Eq.4.1), the velocity of a circular grain decreases to

$$v = M_b\left(g - \frac{\gamma_b}{R}\right) = \frac{3L\ell}{4}(g - \frac{\gamma_b}{R}) \quad \text{(Eq.4.2)}$$

where, R is the radius of the grain. The circular grain might grow or shrink based on its radius size and the dislocation density (and hence the stored energy) in the deformed grain. For the assigned dislocation density, the corresponding critical radius could be determined where a grain with a larger radius grows and grain with a smaller radius shrinks. From Eq. (4.2), and counting for (Eq.3.4), the critical radius could be given by

$$R^c = \frac{\gamma_b}{g} = \frac{2\gamma_b}{\mu b^2 \rho_{eff}} \quad \text{(Eq.4.3)}$$

obviously, a critical dislocation density can be performed instead of the critical radius by considering a particular initial radius of the recrystallized grain. based on this case, the

recrystallized grain will grow only if the dislocation density in the deformed grain will be higher than the critical value, e.g.,

$$\rho_{eff}^{c} = \frac{2\gamma_b}{\mu b^2 R} \quad \text{(Eq.4.4)}$$

4.1.1.1 The growth rate of a recrystallized grain

A few 2D simulations were executed to investigate these specific scenarios by utilizing our phase-field model. The system size was $(1.28\ x\ 1.28)\ microns$ — the interface width set to be 40 nm. Periodic boundary conditions were employed in both directions. Periodic boundary conditions were applied in both directions. From (Eq.4.4), the critical dislocation density that corresponds to the recrystallized grain critical radius ($160\ nm$) is $\rho_{eff}^{c} = 3.3x10^{14}\ m^{-2}$. A three different simulations with different three values for the dislocation density (e.g., $\rho_1 = 2.3x10^{14}\ m^{-2}$, $\rho_2 = 3.3x10^{14}\ m^{-2}$ and $\rho_3 = 4.3x10^{14}\ m^{-2}$) were conducted. As predicted from Eqs. (4.2, 4.3, and 4.4), the recrystallized grains grow if the dislocation density was found to be higher than the critical otherwise, it will shrink. If the dislocation density approached a constant critical value, then the grain radius will remain constant. These sequences were illustrated in Figures 22-23. As can be seen in figure 22, it proves the growth/shrinkage of the recrystallized grain at the expense of the deformed bulk grain. In this figure, a few snapshots of the evolution of a recrystallized grain in the deformed matrix were performed. If the dislocation density in the deformed matrix is higher than the critical value, then the recrystallized grains grow (upper row); but it will shrink if the dislocation density in the deformed grain is below the critical value (lower row). If the dislocation density is precisely equal to the critical value,

then the recrystallized grain will not grow or shrink (middle row), and it will keep at a constant size.

The development/evolution of the recrystallized grain size in the deformed matrix at various values of dislocation densities was represented in Figure 23. Remarking that, the critical dislocation density is ($\rho_{eff}^{c} = 3.3x10^{14}\ m^{-2}$). Then the grain size will increase if the dislocation density higher that this value and decreases if the dislocation density lower than it.

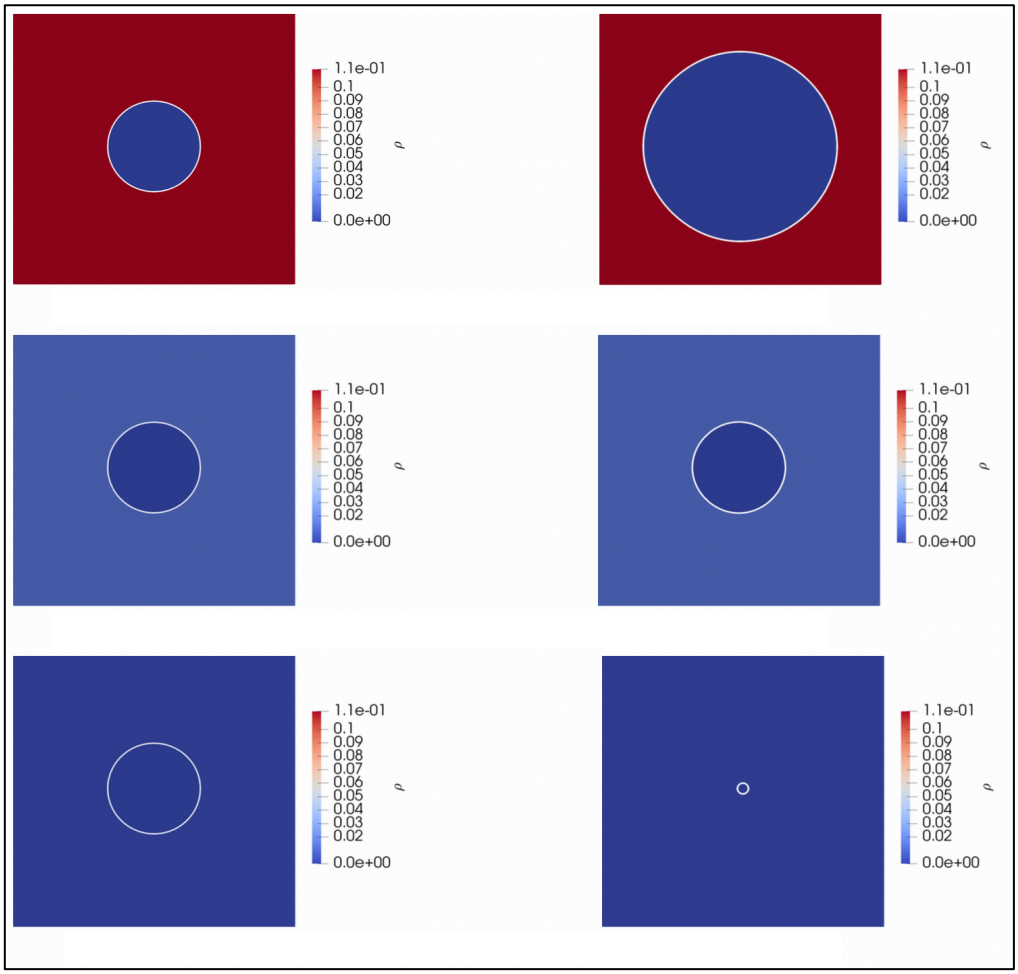

Figure 22 The growth/shrinkage of the recrystallized grain at the expense of the deformed matrix grain.

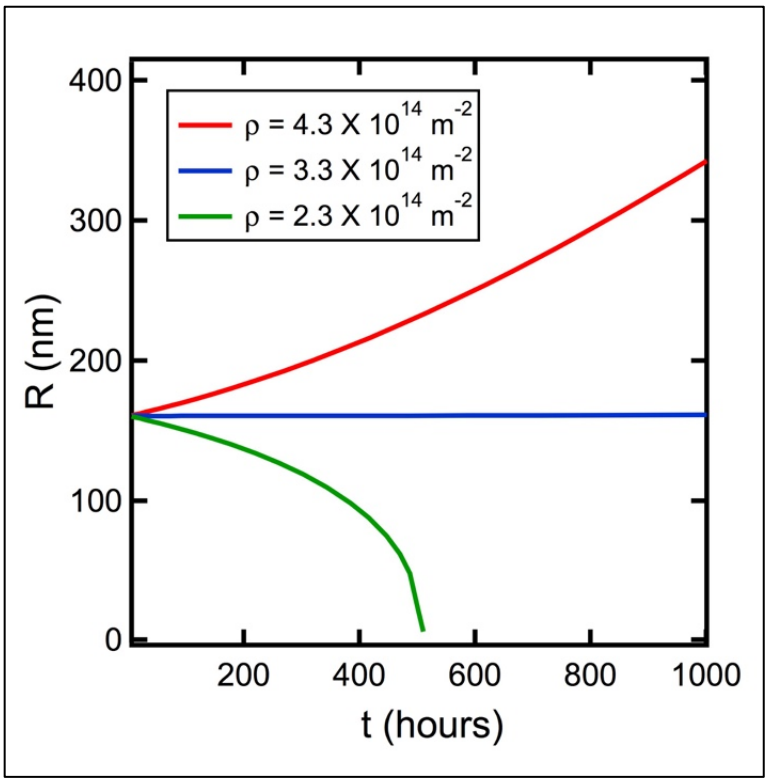

Figure 23 The change of the recrystallized grain radius with time for different dislocation densities

4.1.1.2 Particles pinning the recrystallized grain.

The Second-phase particles exert a drag force on a boundary migration, which hinders the grain boundary velocity. To study the particle-inhibited grain growth, a few theoretical models were introduced in the literature [49, 72-73]. These models can be sorted into two classes (mobile or immobile) based on the way to treating the particles movement. Second-phase particles such as inclusions or precipitates are usually recognized to be immobile, while pores and bubbles are usually reflected as mobile.

4.1.1.2.1 Immobile particles

The impact of immobile particles on the grain growth process was first studied by Zener [47] (as explained and described in section 2.1.2.2.1). By considering a randomly distributed immobile particles with a spherical shape, Zener proposed the curvature to be the driving force for the boundary movement. On the other hand, the particles will exert a drag force which leads to hinder the boundary motion.

(Eq.2.5a) was to present the grain boundary velocity, based on that equation, there are two likely scenarios for the interaction between the immobile particles with the grain boundary. The first case, where the boundary can break away and hence leaves the particles if ($F_b \gg N_p F_b$). Second, if the particle can effectively pin the boundary and halt the grain growth, this can exist under the condition of ($F_b = N_p F_b$).

4.1.1.2.2 Mobile particles

The influence of mobile particles (such as pores or bubbles) on grain growth is more complicated. The boundary migration exerts a force on the particle, and hence the shape of the particles will be changed. Consequently, the particles can easily be dragged by the grain boundary movement [49, 72-73]. The interaction between a mobile particle and a grain boundary could be explained in two different scenarios as well. In one case, the migrating boundary will be splitter away from the particle. In the other case, the migrating boundary could drag the particle onward with it. If the boundary separates from the particle, the boundary moves with its velocity as in the particle-free case [49, 72]. Lastly, the boundary breakaway will simply occur whenever the grain velocity v_b exceeds the particle velocity v_p , i.e. where $M_p F_p < M_b(F_b - N_p F_b)$.

4.1.1.2.3 Particle-grain boundary interaction test case

we conducted a test case to simulate the particle-grain boundary interaction cases. For the case of immobile particles effects on the grain boundary motion, the immobile particles set to have zero mobility. This was illustrated in Figure 24 (first row). The simulation results agree well with the classical Zener model. For immobile particles, multiple small particles pin the boundary more than a few larger particles (this was demonstrated effectively in a larger scale simulation among this work in the HBS results sections). Simply, the immobile particles cases are the opposite to the case of mobile particles [49]. The second case, where the influence of particle drags the kinetics, as shown in figure 24 (second row). As evident from the figure, its clearly describes the quasi- rigid-body motion of the particles along with the boundary, which is regularly considered in the theoretical models.

The last case, where the grain boundary motion having higher velocity, so it can break the mobile or immobile particles, this case can be seen clearly in figure 24 (last row), as the boundary was able to separate far from the particles. This can be explained based on the fact that if fewer pining particles exist, the boundary could wrap around the particles and reduce its size till it approaches the critical driving force/velocity needed to separate from the particles, as observed in experimental micrographs of HBS [11, 17, 49]. Finally, Figure 25 presents the recrystallized circular grain evolving in the case of mobile/immobile second phase particles vs. the case of no particle exist (single-phase).

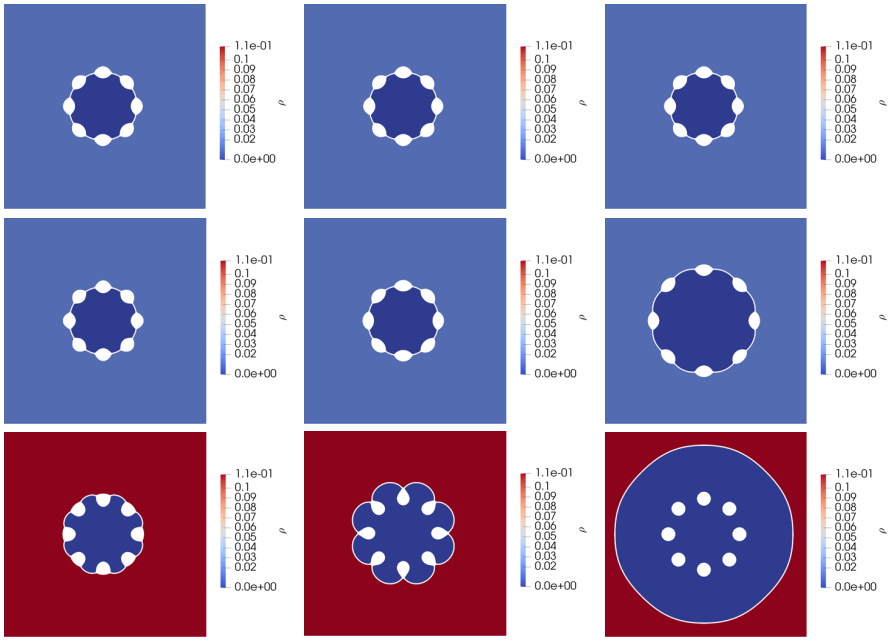

Figure 24 Snapshots to illustrate the three different scenarios of particle-boundary interaction. First row is to show the case of immobile particles effect on the grain boundary motion, the second row presents the particle drags the boundary kinetics case. Finally, the last row was to show the high-velocity grain boundary breaks away from break away from mobile or immobile particles

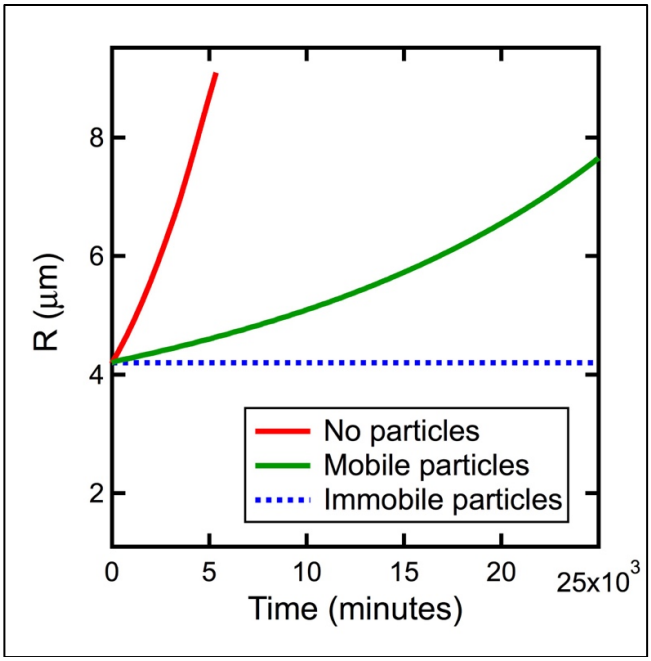

Figure 25 The evolution of grain radius in case of single-phase matrix and mobile/immobile second phase particles.

4.1.2 Irradiation-induced recrystallization for a deformed bicrystal system.

This section will show 2D simulations of irradiation-induced recrystallization in bicrystal systems, these simulations were executed by the initial version of the current model [10, 74]. Usually, there are two famous methods in phase-field modeling to describe the nucleation processes [75]. The classical and the more accurate way is to directly incorporate Langevin type fluctuations in the evolution equations. the second way is to directly add new stable nuclei with a particular rate (estimated from the classical nucleation theory). Both approaches have their own advantages and shortcomings. Here we implemented a simpler version of the first method (where fluctuations considered in the initial conditions). To represent the new grains, we implemented an extra set of order parameters, the added new order parameters evolve via the same evolution equation as the normal order parameter set, which describes the originally deformed grains.

We started by investigating the case of irradiation-induced recrystallization at the boundary of a deformed grain. The system size was $(12.8\ x\ 12.8)\ microns$. The thickness of the initially deformed grains (two grains in this case) was set to be $6.4\ microns$ each; the interface width was taken to be $400\ nm$. Two order parameters represented the two deformed grains and set of four extra order parameters were maintained for the nucleation of new grains description. Various dislocation densities were analyzed to investigate the effect of the dislocation density on the recrystallization process. The nucleation process would be very similar to what we discussed before about the grain-growing (there is a critical dislocation density for a recrystallized grain to grow). Therefore, if the nuclei/grain couldn't grow into stationary size grains, they will eventually

disappear. Indeed, our simulations illustrated that a threshold dislocation density $\rho_{eff}^{c} = 3.3x10^{14}\ m^{-2}$ is required for recrystallization to be initiated.

Figure 26 presents the snapshots of the recrystallization process for two distinct dislocation densities higher than the threshold value, with $\rho_{eff}^{c} = 6.6x10^{14}\ m^{-2}$ (upper row) and $\rho_{eff}^{c} = 3.3x10^{14}\ m^{-2}$ (lower row) at 1200K. The higher the dislocation density, the larger number of recrystallized grains. That demonstrates the theory, which states that there is an energy cost associated with the newly grains initiations. The recrystallized grains will increase until they fully replace the entire domain (full recrystallization, i.e., the recrystallization fraction is unity).

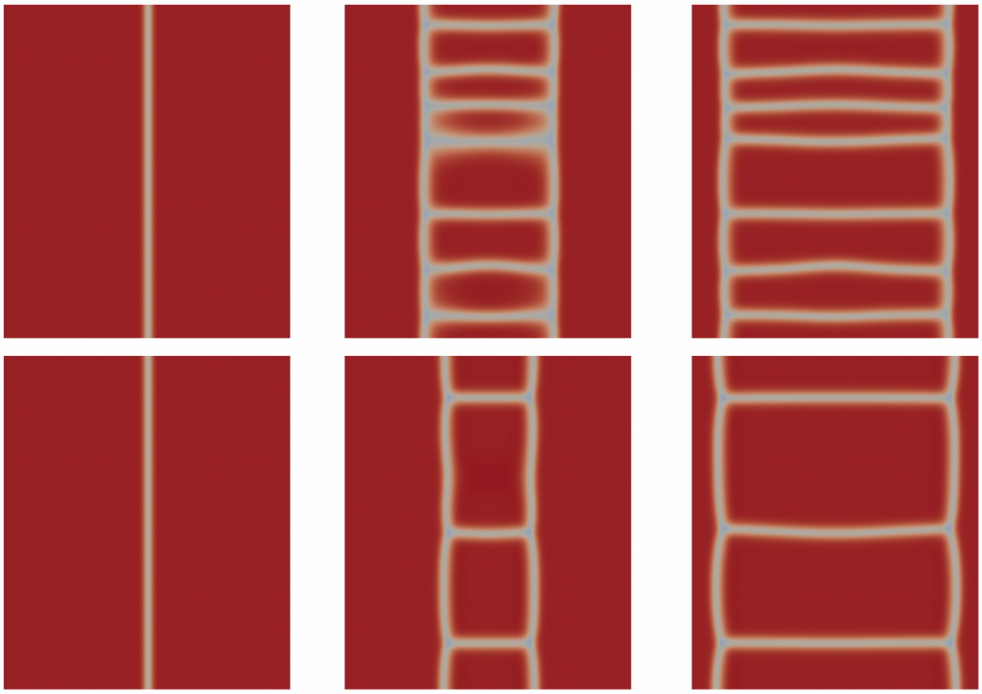

Figure 26 Snapshots of the irradiation-induced recrystallization for an initially deformed UO_2 bicrystal with critical dislocation density of $6.6x10^{14}m^{-2}$ (upper row) and critical dislocation density of $3.3x10^{14}m^{-2}$ (lower row) at 1200K. More recrystallized grains are formed as the dislocation density increases, reprinted from [10].

4.1.2.1 Irradiation-induced recrystallization model to simulate HBS in UO_2

The model employs the HBS formation as a phase transformation process. The initial version of this model [74] demonstrates its capability to simulate the homogeneous (grain subdivision) and heterogeneous (recrystallization) nucleation. to show these capabilities, a simulation test case was executed successfully, and the results presented here as figure 27. The figure displays snapshots of the nucleation and growth of recrystallized grains at several dislocation densities. In this simulation case, the system domain was $(10.24\ x\ 10.24)\ microns$ and grid size was $10\ nm$. For grain subdivision scenario (recrystallization happen everywhere), higher dislocation densities should be performed. For a lower dislocation density ($\rho = 2.2x10^{15}\ m^{-2}$), the recrystallized grains nucleate only at the grain boundary since the nucleation barrier is lower than the matrix as expected from heterogeneous nucleation theory [76].

For an intermediate value of the dislocation density ($\rho = 2.8x10^{15}\ m^{-2}$), the recrystallization starts at the grain boundary first, and then in the deformed bicrystal matrix. But for the high dislocation density ($\rho = 6.2x10^{15}\ m^{-2}$), a sub-grains case will nucleate everywhere in the system (homogeneous nucleation). That shows the capability of our model to simulate both homogeneous and heterogeneous nucleation without any ad hoc or a priori assumptions.

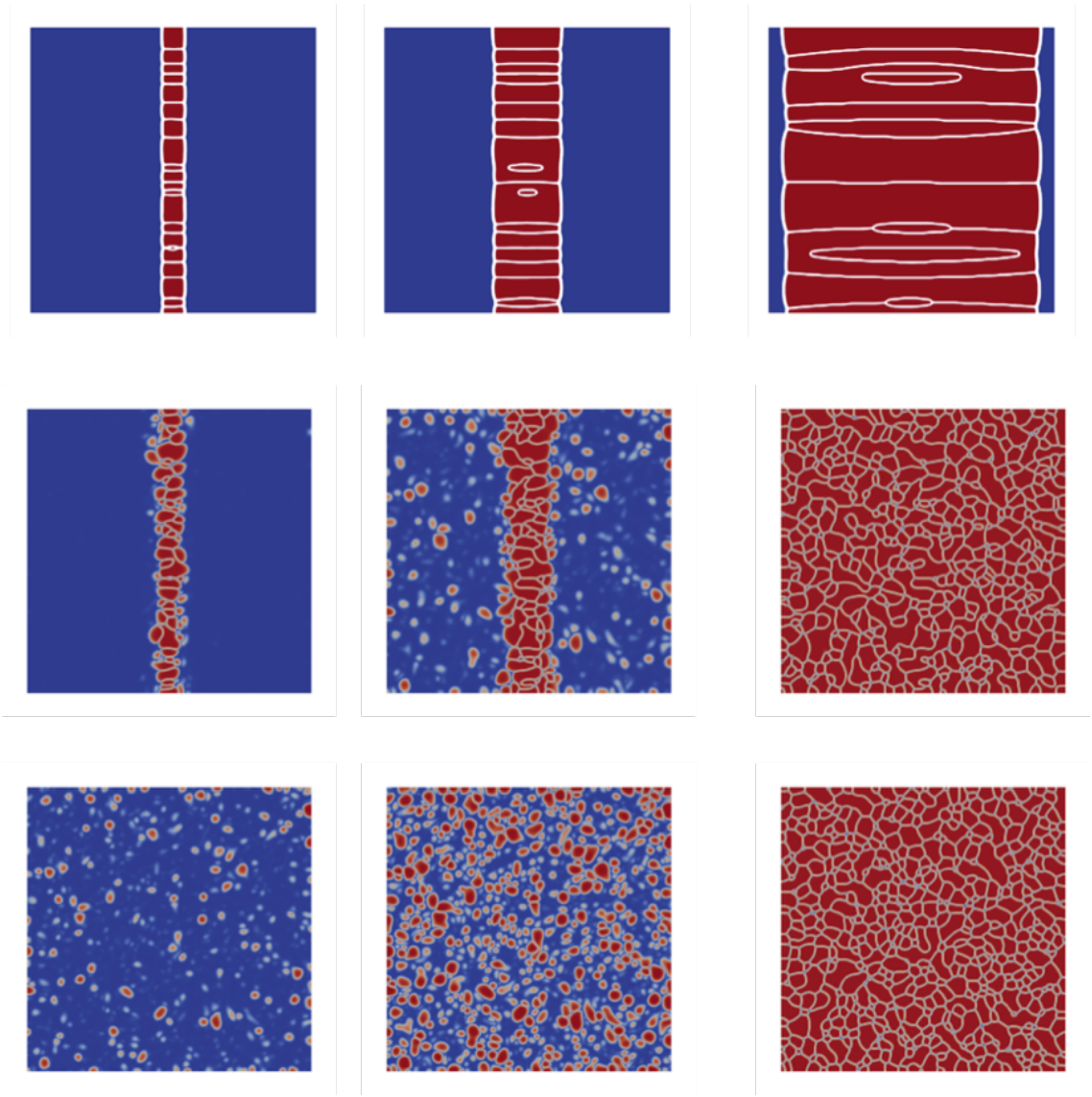

Figure 27 Effect of dislocation density on the heterogeneous nucleation of sub-grains. For the case of low, intermediate and higher dislocation density, reprinted from [74].

4.1.2.2 Interfaces influence on the recrystallization kinetics.

As illustrated in section 2.1.2.4, the solid-solid interface can be classified into three general categories, Coherent, Semi-coherent, and Incoherent interfaces. The coherent interface could be defined as the interface across where lattice planes are continuous.

Incoherent interfaces express the interface where the structure has no lattice plane continuity across the interfaces. The semi-coherent interfaces are not entirely coherent or incoherent and are then typically continuous lattice planes interlarded with discontinuity sites.

We performed several simulation cases to investigate quantitatively the effect of interfaces types on the recrystallization kinetics at Four different bubbles volume fraction (1, 5, 10, and 15 %) with three levels (low, mid and high) of dislocation density (non-dimensionalized), as can be seen in Figure 28. The simulation results successfully captured the behavior of recrystallization kinetics based on the three different bubble-matrix interface types. For the case of coherent interface, the recrystallization rate is the slowest compared to the other two types of interfaces, and it didn't even recrystallize at lower dislocation density. This behavior was predicted as there are no misfits plans associated with the coherent interface and hence no preferable sites for recrystallization to take place. At the medium/high dislocation density, the recrystallization process started to take place, due to the influence of higher dislocation density. The higher dislocation densities give more driving force for the recrystallization to happen, but still, the difference in its rates can be remarked at the coherent interface compared with semi-coherent and coherent interfaces.

One the other hand, the Incoherent interface is considered to have the highest misfit, and therefore the recrystallizations happen faster in all the cases. Finally, the semi-coherent interface, which is the most of real situations, will have lower misfits than the incoherent interface and hence the recrystallization rate in such case usually lies between the corresponding rate of the other two types (coherent and incoherent interfaces).

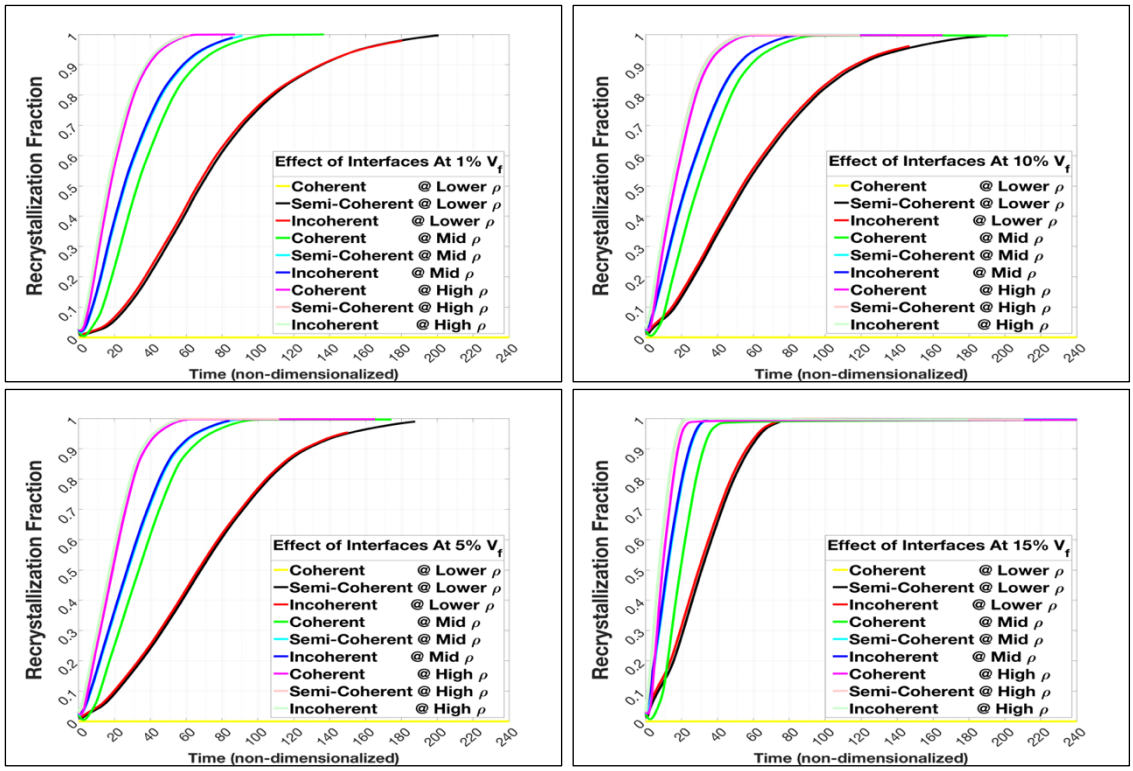

Figure 28 The bubble/matrix interface type influence on the recrystallization Kinetics at different bubbles volume fraction and dislocation densities

4.2 HBS formation and evolution in UO_2[2]

We investigate here the HBS formation and evolution in polycrystalline UO_2. All the simulations presented here were conducted in 2D, to reduce the high computational cost. Furthermore, for simplicity, the production and stochastic terms in Eqs. (3.9.a) and (3.10.a) were set to zero, i.e., nucleation of bubbles was ignored and only their effect on the initiation of HBS transformation was considered. The effects of dislocation density magnitude and distribution, initial grain size, and bubble radius and number density were systematically studied. The simulations proved a strong influence of these parameters on the overall kinetics of HBS formation. Moreover, it was demonstrated that these parameters control the resultant microstructure of the HBS, and hence its thermal and mechanical properties.

4.2.1 Effects of dislocation density and grain size on HBS formation in UO_2

Several simulations were conducted to understand the formation and evolution of HBS in polycrystalline UO_2. The simulations utilize a 2D domain of size $20.48\ by\ 20.48\ microns$, with an average grid size of $20\ nm$. The initial size of the damaged grains was varied between $2.9 - 4.1\ microns$. For simplicity, in most simulations, all the initial grains were assumed to be damaged and to have the same

[2] Reprinted with permission from springer "Mesoscale Modeling of High Burn-Up Structure Formation and Evolution in UO2" by M. Gomaa Abdoelatef, Fergany Badry, Daniel Schwen, Cody Permann, Yongfeng Zhang, and Karim Ahmed, 2019. JOM, Copyright [2019] by The Minerals, Metals & Materials Society (JOM).

dislocation density. However, the effect of non-uniform dislocation density was also studied.

First, we investigate the effect of the magnitude of the dislocation density on the process of HBS formation and evolution. This is captured in Figure 29 that represents snapshots of the HBS formation and evolution. Due to the high computational cost, the initial grain size of the damaged grains was set to be 2.9 $microns$, which is close to the initial grain size range in UO_2 pellets ($5 - 10\ microns$) [14]. As evident from the figure, the value of the dislocation density affects both the size and morphology of the recrystallized grains. A critical dislocation density was found below which no recrystallization takes place. The value of this critical dislocation density is $\rho_{eff} = 5.17x10^{14}\ m^{-2}$ or equivalently 41 GWd/tHM burn-up. As the dislocation density increases (from the upper row $\rho_{eff} = 6.25x10^{14}\ m^{-2}$ or 45 GWd/tHM burn-up to the lower row $\rho_{eff} = 2.50x10^{15}\ m^{-2}$ or 72 GWd/tHM burn-up), the recrystallized grain size decreases and the number of recrystallized grains increases. This is consistent with the fact that the critical radius is inversely proportional to the strain energy difference between the damaged and recrystallized grains. Moreover, as the dislocation density increases, the morphology of the recrystallized grains changes from coarse equiaxed grains at low values of the dislocation density $\rho_{eff} = 6.25x10^{14}\ m^{-2}$ to columnar grains at intermediate values $\rho_{eff} = 1.33x10^{15}\ m^{-2}$ to fine equiaxed grains at high values $\rho_{eff} = 2.50x10^{15}\ m^{-2}$. Furthermore, the heterogeneous nature of recrystallization is sensitive to the magnitude of dislocation density as manifested in Figure 29, as well.

For low values of the dislocation density, recrystallization proceeds only at triple- and higher order-junctions (upper row). At intermediate values, recrystallization also takes place at the grain boundaries (second row). At high enough dislocation density, new sub-grains form at the boundaries of the just recrystallized grains (third row). The grain subdivision, where nucleation of new grains can occur inside the bulk of damaged grains, starts to take place at higher dislocation density (fourth row). Note that the model correctly reproduces the different morphologies of grains recrystallized at different junctions, e.g., two, triple, and higher-order junctions. All these results are consistent with the heterogeneous nucleation theory. This is a major strength of our model where nucleation of recrystallization is treated explicitly and no a priori assumptions on the nucleation rate and sites or the size and morphology of the recrystallized grains are required. The range of dislocation or equivalently burn-up predicted here for HBS formation in UO_2 fuel agrees well with the experimental data reported in the literature[11, 14, 32-33].

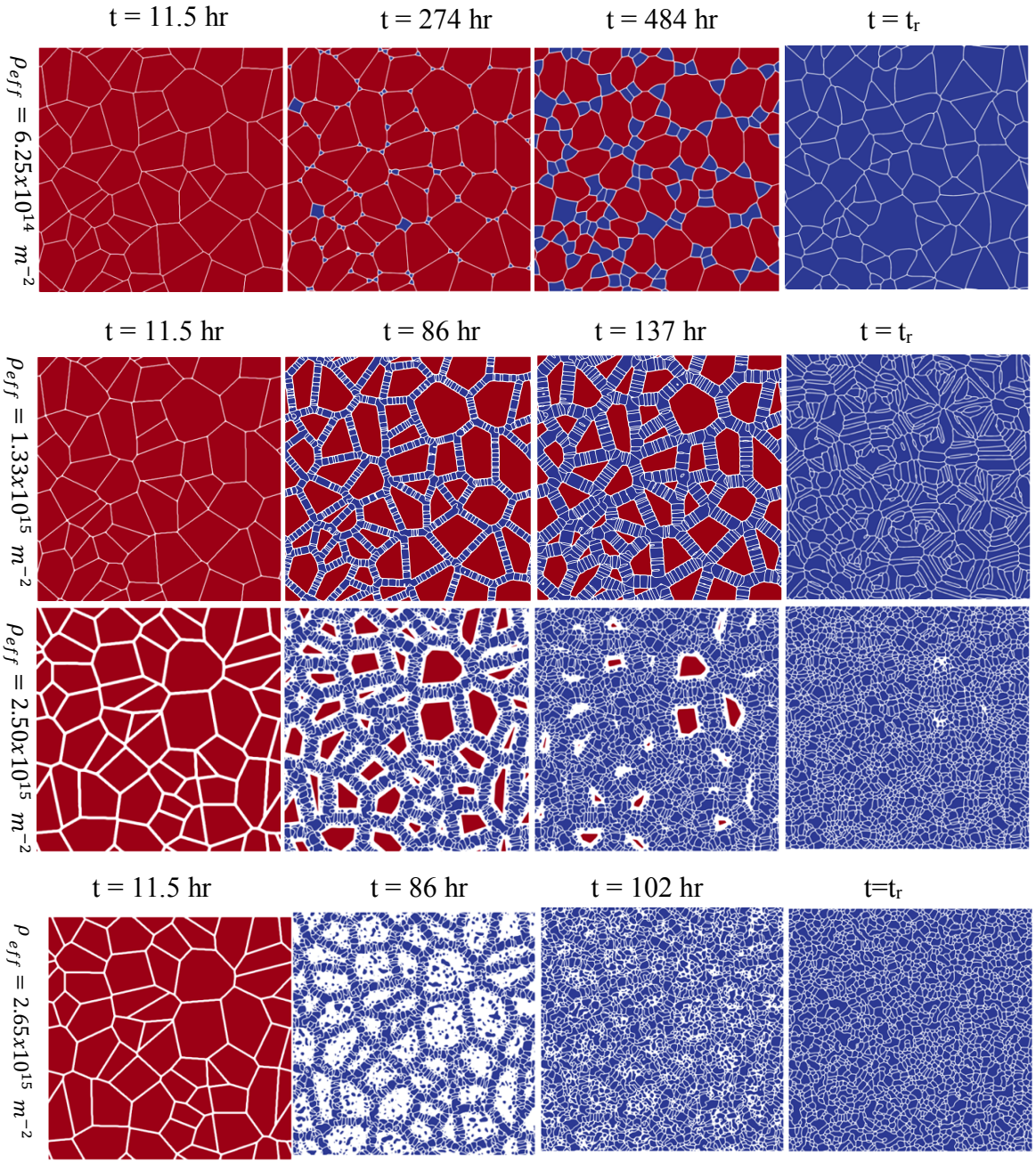

Figure 29 Effect of dislocation density on irradiation-induced recrystallization in polycrystalline UO_2 at 1200K. The initially damaged grains are presented in red color and the recrystallized (dislocation-free) grains in blue. t_r is the time at which recrystallization is complete. The dislocation density increases from the upper row to the lower row. The recrystallization time (t_r) reduces with increasing dislocation density (see Figure 30).

The effect of dislocation density on the overall kinetics of HBS formation in polycrystalline UO_2 is quantitatively shown in figure 30. At very low dislocation density ($\rho_{eff} = 5.00\ x10^{14}\ m^{-2}$) no recrystallization takes place, but higher dislocation density leads to shorter incubation time and faster recrystallization kinetics (as evident from Figure 30a). Moreover, higher dislocation density results in a larger number of recrystallized grains, and hence smaller average grain size (as can be seen from Figure 30b). This is in a good agreement with expectations from the classical nucleation theory [76]. Note that after recrystallization is completed, regular grain growth, where the number of grains decreases and grain size increases, takes place. For the cases where the resultant microstructure resembles the HBS micrographs, i.e., when it develops uniform and fine grain structures, the recrystallized average grain size was found to lie within the range of $0.3\ to\ 0.5\ microns$ corresponding to a range of dislocation densities of $\rho = (2.5x10^{15} - 2.65x10^{15})\ m^{-2}$ (or equivalently a burn-up of 70-75 GWd/tHM). These ranges of grain size and burn-up agree well with the reported values [11, 14, 32-33].

We then studied the effect of the grain size of polycrystalline UO_2 on the kinetics of HBS formation. The investigation considered two different initial grain sizes of $2.9\ and\ 4.1\ microns$ at a dislocation density of $\rho = 1.33x10^{15}\ m^{-2}$. The results of these simulations are presented in Figure 31. As can be concluded from this figure, the recrystallization proceeds faster with decreasing grain size. This is due to the fact that the smaller grain size leads to higher grain boundary area per unit volume, and hence more preferable nucleation sites. Moreover, the trend predicted here agrees with the experimental date reported for UO_2 [11, 32-33].

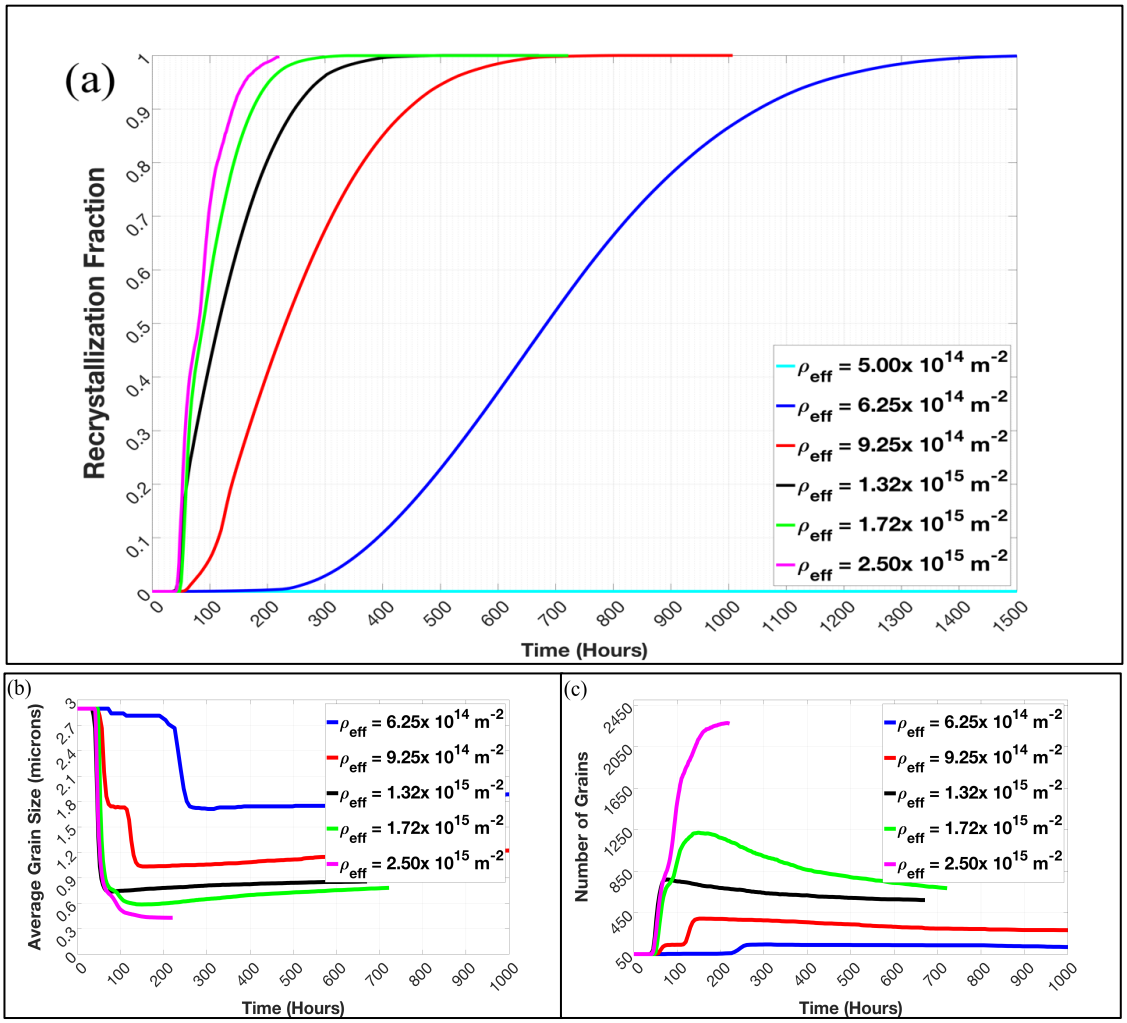

Figure 30 Effect of dislocation density on the kinetics of recrystallization in polycrystalline UO_2 at 1200K (a) the increase of the recrystallization fraction with time (b) the evolution of the average grain size and (c) the change in the total number of grains with time.

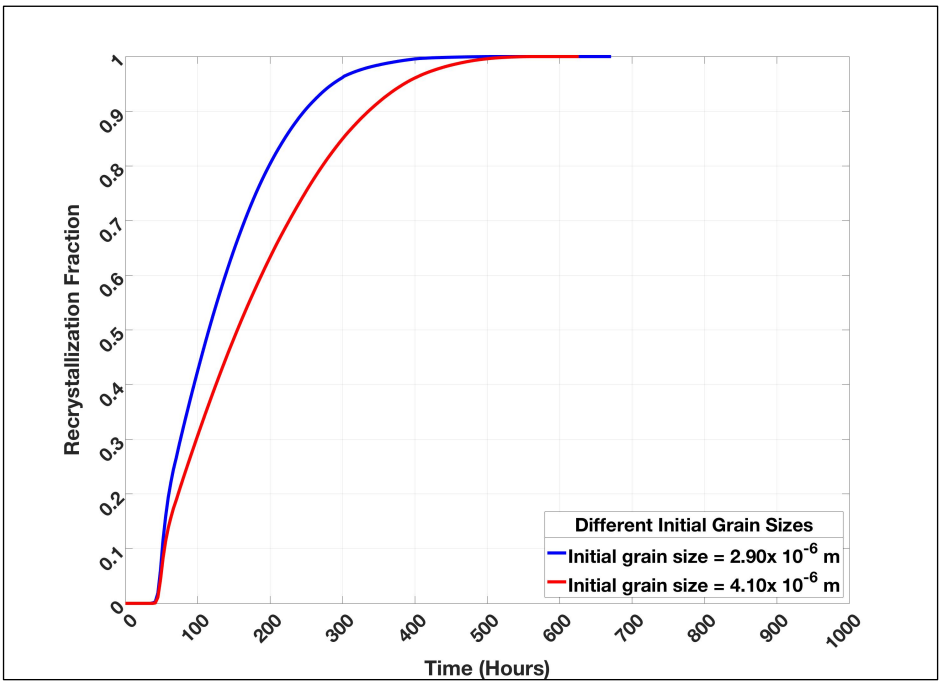

Figure 31 Effect of the initial grain size on the recrystallization kinetics. Faster recrystallization kinetics is observed for smaller grain size due to the higher density of nucleation sites.

4.2.2 Effect of the distribution of dislocation density

In the simulations above, it was assumed that the dislocation density is uniform and constant in all grains. However, this is unrealistic in most situations. For instance, under non-uniform applied mechanical load or irradiation, the heterogeneous distribution of dislocations is expected. For UO_2 pellets, it is known that irradiation damage is more pronounced at the periphery than in the center of the pellet. That is due to the difference in the fission density between those regions. Additionally, the high temperature at the center, leads to the annealing of defects. i.e., Irradiation damage and recovery take place almost simultaneously at the center of the pellet. Moreover, the stresses arising from the temperature gradient across the pellet center also contribute to the heterogeneity of

irradiation damage. Hence, it is expected that the dislocation density will be higher at the periphery than in the center.

We investigate the effect of non-uniform dislocation density by assigning a spatially dependent dislocation density. To approximate the distribution of dislocations in UO_2 pellets, we assign a linear profile for the dislocation density along the radius. This is shown in Figure 32 that represents the HBS formation in polycrystalline UO_2 pellets. At the center of the domain, the dislocation density was set to $\rho = 6.25x10^{14}\ m^{-2}$ (0.25 in the figure as a non-dimentionalized value). The dislocation density attained its maximum value $\rho = 2.5x10^{15}\ m^{-2}$ (1.00 in the figure as a non-dimentionalized value) at the corners of the domain. As can readily be inferred from the figure, the non-uniform distribution of dislocations leads in turn to a heterogeneous HBS. The recrystallized grain size, orientation, and morphology change drastically along the radius. This is consistent with the above results that demonstrated a strong effect of the value of the dislocation density. This will eventually result in non-uniform mechanical and thermal properties along the radius as was reported before [14].

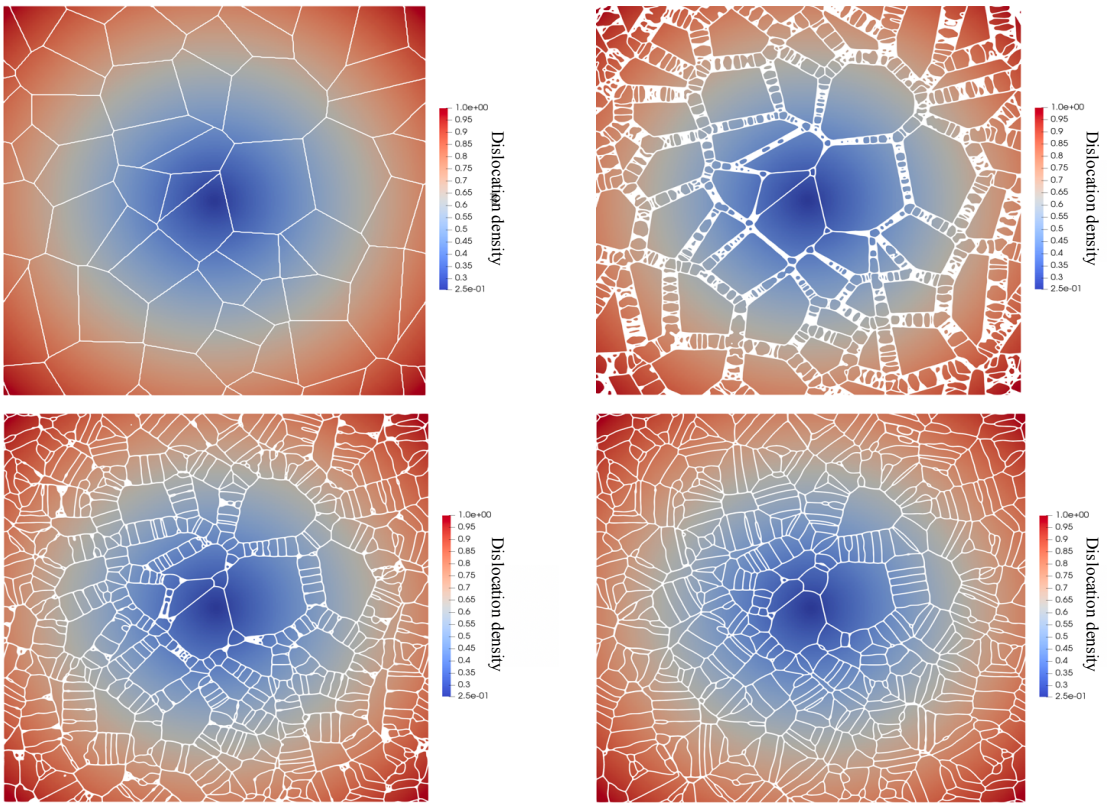

Figure 32 A Simulation of HBS formation in a UO_2 pellet. The dislocation density changes radially, i.e., it is lowest in the center and highest at the periphery (see text for exact numbers). Only the grain boundaries and the initial dislocation distribution are shown here for better visualization. Time progresses from top left to bottom right.

4.2.3 Effect of gas bubbles on the kinetics of HBS formation

We turn our attention to the effect of bubbles on the kinetics of recrystallization in polycrystalline UO_2. It was reported several times that bubbles formation often precedes recrystallization during HBS formation in UO_2. Moreover, it is well-known that second-phase particles in general strongly influence the overall kinetics of both recrystallization and grain growth in materials, as explained in the reviewing chapter (Chapter two, in this work). On one hand, they act as nucleation sites, leading to enhance the kinetics of the

recrystallization. On the other hand, they also act as pinning sites for the gain boundaries, resulting in hindered grain growth kinetics. To investigate the effect of bubbles on the HBS formation in UO_2, we performed several simulations with different bubble configurations. The results of these simulations are summarized in figures 33-35.

Snapshots of HBS formation and evolution are shown in Figure 33. The number of bubbles and bubble radius were varied to investigate their effects on the process. The initial grain size of $2.9\,microns$ and a relatively low dislocation density of $\rho = 6.25x10^{14}\ m^{-2}$ were used. As evident from figure 33, the presence of bubbles enhances the kinetics of recrystallization in all cases. It is worth noting that the model correctly reproduces the different equilibrium morpholgies of bubbles and recrystallized grains. The equilibrium morpholgy is determined through the establishment of the equilibrium dihedral angle at the bubble/grain tips/triple-junctions. Moreover, the model predicts that the grains recrystallized near the bubbles tend to wrap around the surface of the bubbles (as investigated in the result test caseses section) that act as a surface defect, and hence a preferred nucleation site. This was observed in experimental micrographs of HBS [11, 17]. Furthermore, the model can also concurrently simulate grain growth and particle coarsening if simulations were to run for longer times as in [65, 71].

The effects of gas bubbles on the overall kinetics of recrystallization in polycrystalline UO_2 are quantitatively summarized in figures 34 and 35. Figure 34 represents the recrystallization rates at different dislocation densities for two distinct bubble configurations with the same area fraction. Figure 35 shows the recrystallization rates at different dislocation densities for two distinct bubble configurations with the same

radius and different number density. As represented in the figures, the recrystallization rate increases with bubble number density. The enhancement is more pronounced at lower dislocation densities. This is consistent with the fact that bubbles provide extra nucleation sites for recrystallization to take place. The effect of the bubble radius was also studied but was found negligible compared to the number density. Nonetheless, the effect of bubble radius is expected to have a more pronounced effect on the later grain growth kinetics (after recrystallization is complete), as demonstarted before in previous studies [65-66, 71].

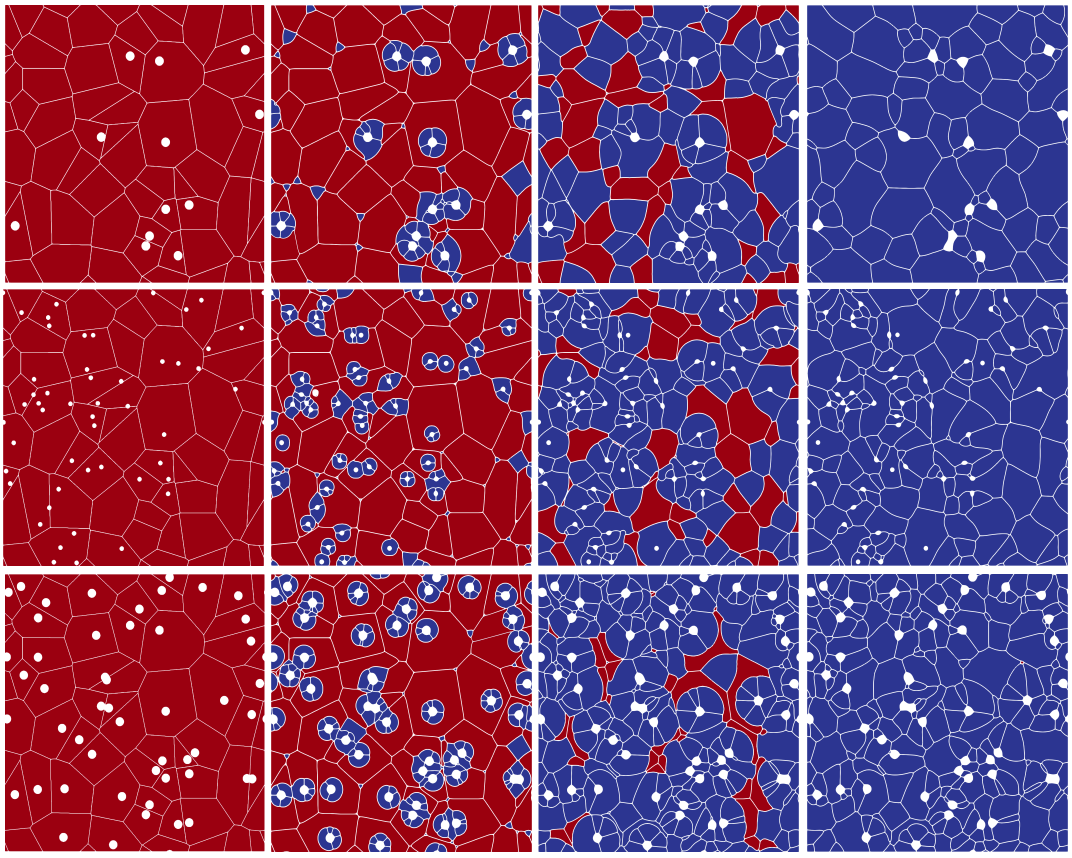

Figure 33 Effect of gas bubbles on the recrystallization kinetics in polycrystalline UO_2 at 1200K. The first and second rows have the same bubble area fraction. The second and third rows have the same number of bubbles. In all configurations, bubbles tend to accelerate the overall kinetics of recrystallization by providing extra nucleation sites. It is worth noting that grains recrystallized at the bubble surface have different morphologies from those at grain junctions. Moreover, the model also captures bubble merging (coarsening) during grain growth (see the last column).

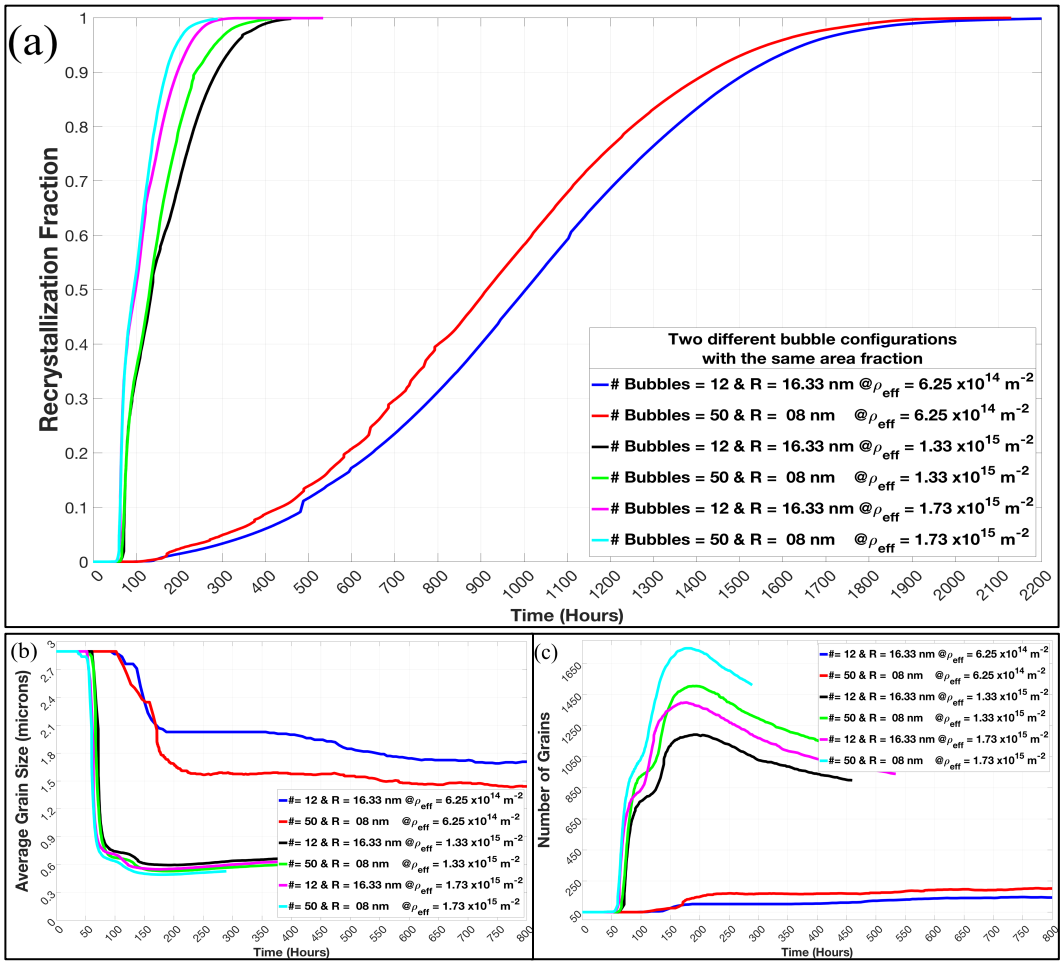

Figure 34 Effect of gas bubbles on (a) the recrystallization kinetics in polycrystalline UO_2, (b) Average grain size and (c) Number of grains. Two different bubble configurations with the same area fraction at different dislocation densities were considered. In all cases, gas bubbles increase the recrystallization rate. This increase is more pronounced at lower dislocation densities. For the same bubble area fraction and dislocation density, configurations with the higher number of bubbles recrystallize faster.

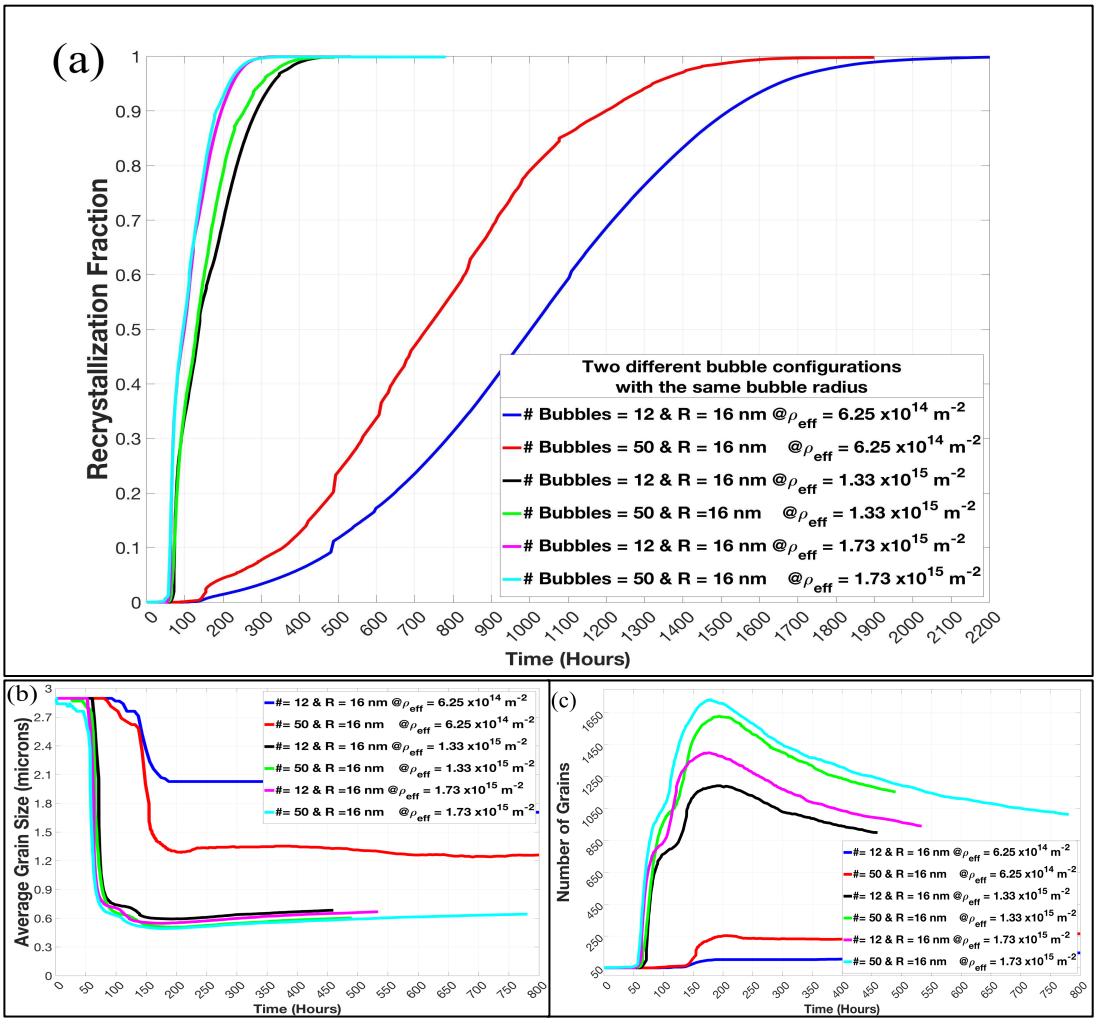

Figure 35 Effect of bubble number density on (a) recrystallization rate in polycrystalline UO_2 (b) average grain size and (c) number of grains. For the same bubble radius and dislocation density, a higher number of bubbles leads to enhanced recrystallization kinetics. This enhancement is more apparent at lower dislocation densities.

4.3 HBS formation and evolution in U-Mo dispersion fuel

Various 2D simulations of HBS formation and evolution in U-Mo were conducted in this results part. the first case was to study the single-phase (with no bubbles existing) recrystallization kinetics. Additionally, the influences of the Fission density magnitude and initial grain size on the recrystallization were executed. Finally, the recrystallization in case of second-phase particles (gas bubbles) was examined. The system size was the same as used in UO_2 simulations (20.48 by 20.48 microns) and the grid size was setted to be (20 nm). All initial grains (50 grains, with 2.9 microns grain size) were considered to be deformed (the same dislocation density was uniformly distributed among the matrix). The Grain Tracker algorithm was employed to examine the original deformed grains and the recrystallizing new grains [8, 34]. lastly, adaptive time and mesh steps were used to decrease the computational cost.

4.3.1 Fission density influence on HBS formation in U-Mo dispersion fuel

The influence of fission density on the recrystallization was studied quantitatively, as shown in Figure 36.a. As can be seen obviously out of the figure, by increasing the fission density, the recrystallization rate will occur faster. Furthermore, the average amount of the recrystallized new sub-grains will increase with higher dislocation density. Consequently, the average grain size reduces (see figures 36.b). This also agrees strongly with the predictions from classical nucleation theory as the average number of recrystallized grains is inversely proportional to the driving force (strain energy associated with dislocations) of nucleation [76].

The quantitative results of recrystallization in U-Mo are in reasonably good agreement with other models prediction and experimental data in the literature [8, 13, 24]. As can be found out from figure 36.b, the phase-field model predicts a critical grain size to lie within a range of $0.3\ microns$ at fission density of $f = 5.50x10^{21}cm^3$ which is corresponding to the burn-up in the range of ~120 GWd/tHM [8, 13, 24-25, 34].

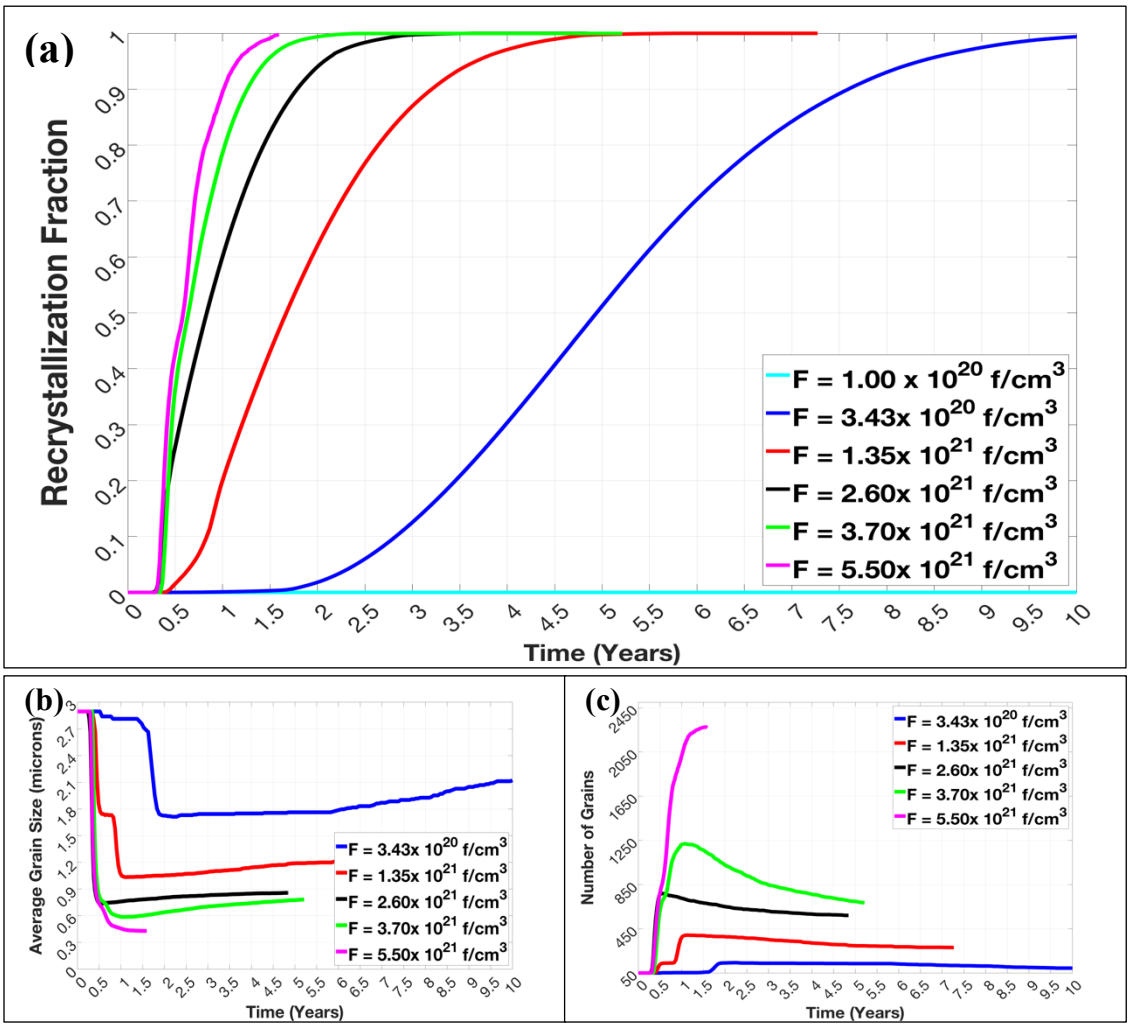

Figure 36 Effect of fission density on the kinetics of recrystallization in U-Mo (a) the increase of the recrystallization fraction with time (b) the evolution of the average grain size and (c) the change in the total number of grains with time.

4.3.2 Grain size influence on HBS formation in U-Mo

We studied the impact of the initial grain size on the recrystallization process in U-Mo. The system size was established as the previous simulation with fission density of ($f = 2.60x10^{21} cm^3$). Two distinct initial grain size cases were investigated. The first case, where the initial grain size was set to be 2.9 $microns$ and the second case, the average grain size was 4.1 $microns$. The effect of initial grain size on the recrystallization is illustrated in Figure 37. Out of this figure, the recrystallization kinetics moves faster with reducing the grain size. This well agreed with the fact that the specimen with smaller grain size has more grain boundary per unit volume and consequently more preferable nucleation sites

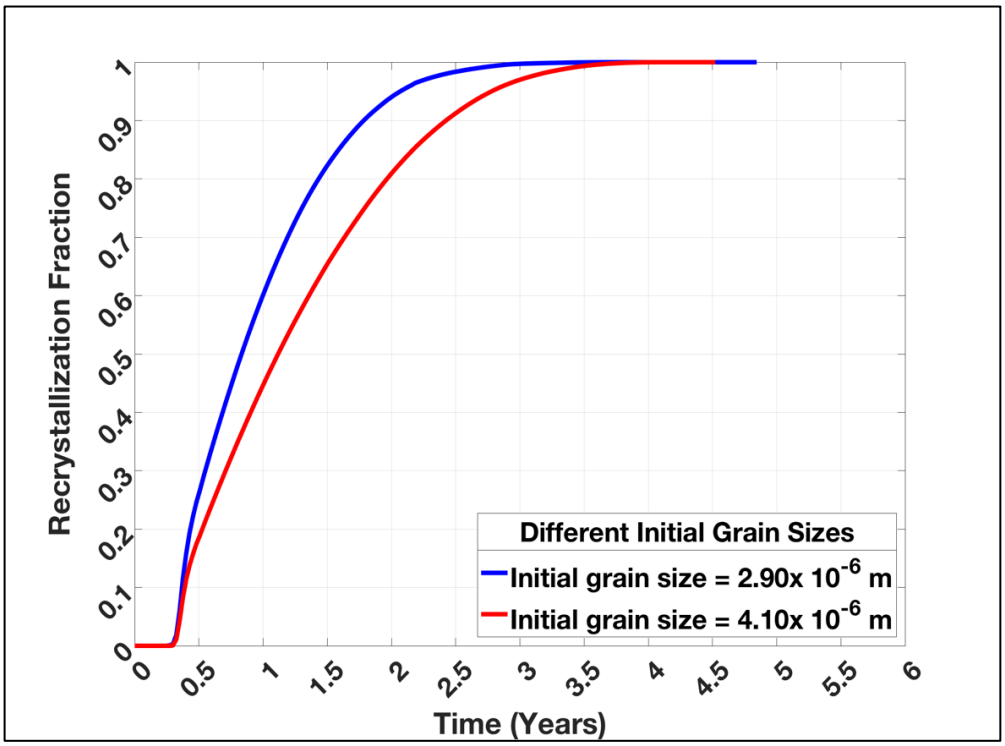

Figure 37 Effect of the initial grain size on the recrystallization kinetics. Faster recrystallization kinetics is observed for smaller grain size due to the higher density of nucleation sites.

4.3.3 Gas bubbles effect on HBS kinetics in U-Mo dispersion fuel

The latest few simulations presented in this work were assigned to study the influence of the bubbles on the recrystallization process in U-Mo dispersion fuel. These investigations were basically to study the impact of bubbles existence on the HBS formation in U-Mo. In that case and according to heterogeneous nucleation theory, the nucleation will start first at the bubble surface, followed by the triple-junction, then grain boundary, and finally will occur in the bulk, if the fission density rises to higher values. The domain size was similar as previously described and the initial grain size (the deformed grains) set to be 2.9 microns [8]. Those simulations were executed with different bubble configurations. The results of these simulations are summarized in figures 38-39.

Figure 38 expresses the recrystallization rates at various fission densities for two different bubble configurations with the identical area fraction. Figure 39 shows the recrystallization rates at various fission densities for two different bubble configurations with the same radius and various amounts. As expressed out of the figures, the recrystallization kinetics rises with bubble number density increases. The enhancement is more noticeable at lower fission densities. This is consistent with the fact that bubbles provide extra nucleation places for recrystallization to occur.

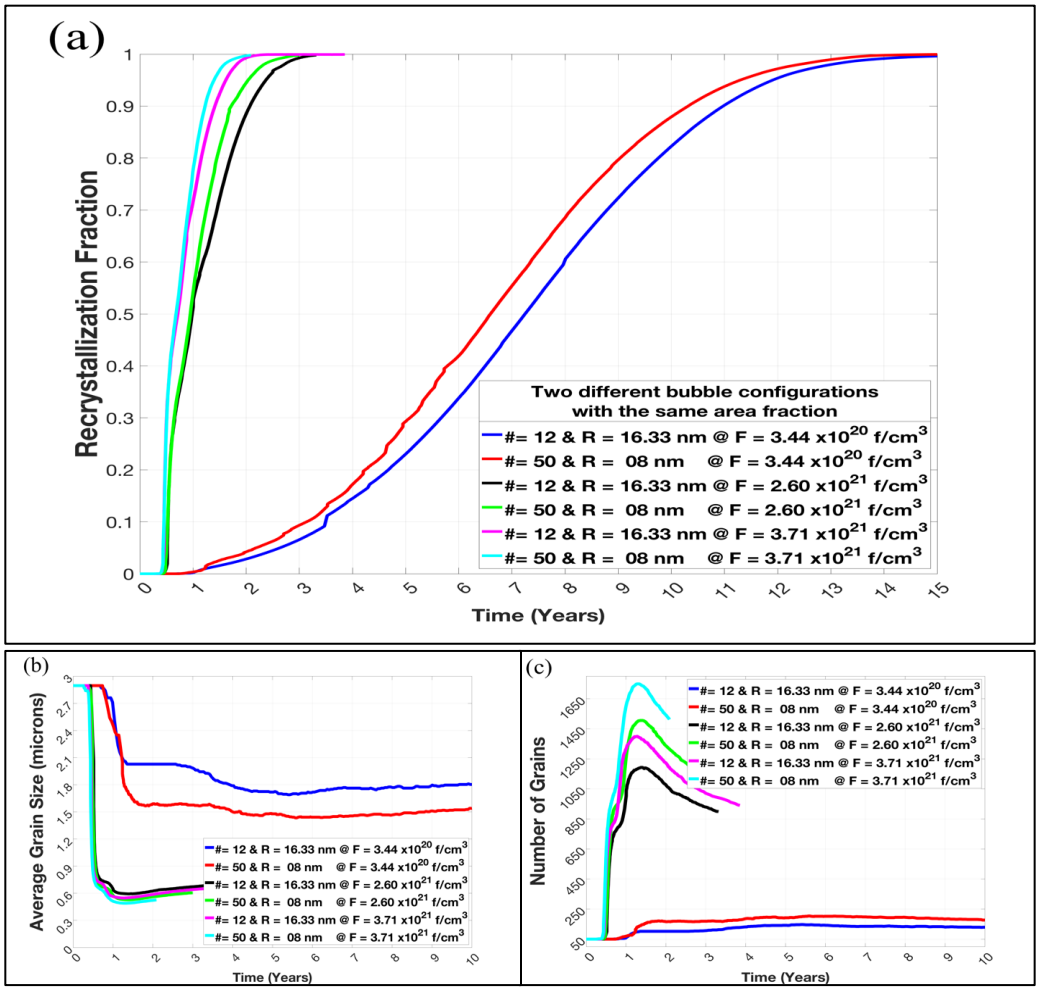

Figure 38 Effect of gas bubbles on (a) the recrystallization kinetics in polycrystalline U-Mo, (b) Average grain size and (c) Number of grains. Two different bubble configurations with the same area fraction at different dislocation densities were considered. In all cases, gas bubbles increase the recrystallization rate. This increase is more pronounced at lower dislocation densities. For the same bubble area fraction and dislocation density, configurations with the higher number of bubbles recrystallize faster.

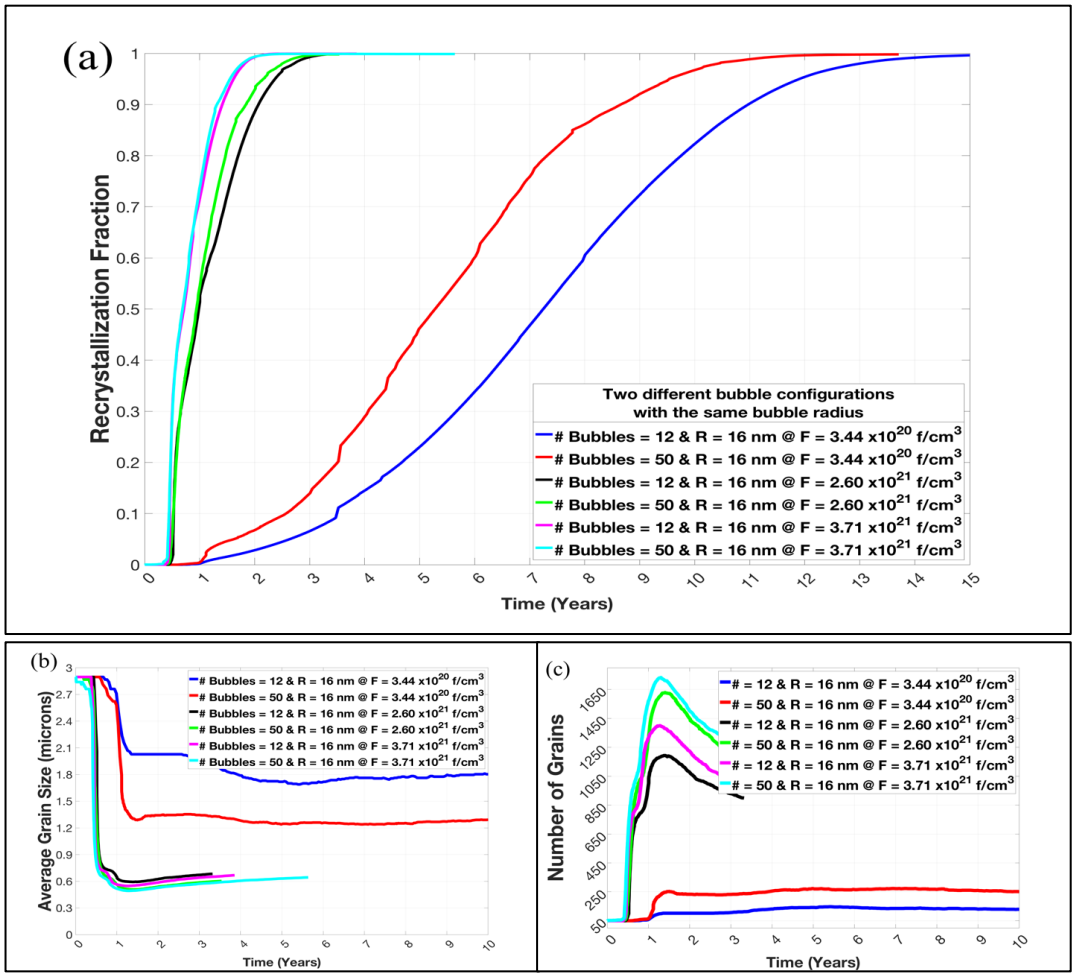

Figure 39 Effect of bubble number density on (a) recrystallization rate in polycrystalline U-Mo (b) average grain size and (c) number of grains. For the same bubble radius and dislocation density, a higher number of bubbles leads to enhanced recrystallization kinetics. This enhancement is more apparent at lower dislocation densities.

CHAPTER V

SUMMARY AND FUTURE DIRECTIONS

5.1 Summary

A quantitative phase field model was introduced for investigating the Irradiation-induced recrystallization and the high burn-up structure formation and evolution in polycrystalline nuclear fuel (UO_2 and U-Mo). The model directly simulates the nucleation of recrystallization, eliminating the need for making a priori assumptions and implementing separate algorithms to model formation of sub-grains. The model accounts for the effects of the magnitude and distribution of dislocations on the HBS. In addition, the model considers the influence of bubbles on HBS formation and evolution. The kinetic evolution equations of the model were solved using a fully coupled and fully implicit scheme implemented in the MOOSE framework.

The simulations showed that the magnitude and distributions of dislocations and bubble number density control the overall kinetics of HBS formation. Moreover, these factors also determine the resultant microstructure of the HBS, and hence its physical properties. The model prediction for the threshold dislocation density related to the HBS formation was found to be in good agreement with theory and experiments. For polycrystalline UO_2 at 1200K, the recrystallized average grain size was found to be on the order of 0.4 microns at a dislocation density of $\rho = 2.50x10^{15}\ m^{-2}$ (or equivalently a burn-up of 72 GWd/tHM), which lies within the range of values reported in [11, 14, 32-33]. The model was able to predict successfully the range of fission density in U-Mo case, which lies within the values of $f = 5.50x10^{21} cm^3$ that corresponds to burn-up in the

range of ~120 GWd/tHM [8, 13, 24-25, 34]. We expect the agreement to be improved when we conduct full 3D simulations.

5.2 Future Directions

The model currently can only account for the effect of grain size and temperature on the kinetics of the HBS evolution. However, the model currently ignores the effect of grain size and temperature on the accumulation of dislocations. Nonetheless, this limitation can be alleviated by coupling the current phase-field model to a rate-theory model of irradiation damage. This will be the subject of future work. Moreover, in future studies, the heat and momentum balance equations will be coupled to the microstructure evolution equations to directly investigate the coevolution of microstructure and thermal and mechanical properties of HBS. This can be accomplished using MOOSE in a straightforward manner [77]. Moreover, the nucleation of gas bubbles, bubble swelling, and gas release will be incorporated into the model. Furthermore, full 3D simulations will be performed. This will provide a mechanistic mesoscale model capable of predicting HBS formation and evolution along with physical properties changes in current and future nuclear fuels. Finally, Our Model will be connected to a Machine Learning (ML) Algorism, hence it will accelerate the simulating time. The proposed approach will be based on implementing a physics-based model that can learn from a ML Algorism.

REFERENCES

[1] Mark. Easton, and D. StJohn, "Grain Refinement of Aluminum Alloys: Part I. The Nucleant and Solute Paradigms—A Review of the Literature," *METALLURGICAL And Materials Transactions A,* vol. 30, no. 6, pp. 1613-1623, 1999.

[2] S. M. Robert W. Balluffi, Kinetics of Materials, New Jersey: John Wiley and Sons Inc, 2005.

[3] E. J. Mittemeijer, Fundamentals of Materials Science, The Microstructure–Property Relationship Using Metals as Model Systems, Germany: springer, 2010.

[4] R.D. Doherty, D.A. Hughes, F.J. Humphreys, J.J. Jonas, D. Juul Jensen, M.E. Kassner, W.E. King, T.R. McNelley, H.J. McQueen, and A.D. Rollett, "Current issues in recrystallization: a review," *Materials Science and Engineering,* vol. 238, pp. 219-274, 1997.

[5] Gary. S. Was, Fundamentals of Radiation Materials Science, Berlin: Springer, 2007.

[6] Patterson, Y. Liu and B. R. 1993, "Grain growth inhibition by porosity," *Acta Metallurgica et Materialia,* vol. 41, no. 9, pp. 2651-2656, 1993.

[7] DR., Olander, Fundamental Aspects of Nuclear Reactor Fuel Element, Washington DC: US DOE, 1976.

[8] A. Leenaers, W. Van Renterghem and S. Van den Berghe, "High burn-up structure of U(Mo) dispersion fuel," *Journal of Nuclear Materials,* vol. 476, pp. 218-230, 2016.

[9] A. Leenaers, S. van den Berghe, E. Koonen, V. Kuzminov and C. detavernier, "Fuel swelling and interaction layer formation in the SELENIUM Si and ZrN coated U(Mo) dispersion fuel plates irradiated at high power in BR2," *Journal of Nuclear Materials,* vol. 458, pp. 380-393, 2015.

[10] K Ahmed, X. Bai, Y. Zhang B. Biner. 2016, "High-Burnup-Structure (HBS): Model Development in MARMOT for HBS Formation and Stability Under Radiation and High Temperature," Idaho, 2016.

[11] K. Nogita, K. Une, "Irradiation-induced recrystallization in high burnup UO_2 fuel," *Journal of Nuclear Materials,* vol. 226, pp. 302-310, 1995.

[12] K. Nogita, K. Une M. Hirai, K. Ito, K. Ito, y. Shirai, "Effect of grain size on recrystallization in high burnup fuel pellets," *Journalof Nuclear Materials,* vol. 248, pp. 196-203, 1997.

[13] Yeon SooKim, G.L.Hofman and J.S.Cheon, "Recrystallization and fission-gas-bubble swelling of U–Mo fuel," *Journal of Nuclear Materials,* vol. 436, pp. 14-22, 2013.

[14] Wiss, Vincenzo V. Rondinella and Thierry. 2010, " The high burn-up structure in nuclear fuel," *Materials Today,* vol. 13, no. 12, pp. 24-32, 2010.

[15] J. Spino, K. Vennix, M. Coquerelle, "Detailed characterisation of the rim microstructure in PWR fuels in the burn-up range 40–67 GWd/tM," *Journal of Nuclear Materials,* vol. 231, pp. 179-190, 1996.

[16] J. Noirot, L. Desgranges, J. Lamontagne, "Detailed characterisations of high burn-up structures in oxide fuels," *Journal of Nuclear Materials ,* vol. 372, pp. 318-339, 2008.

[17] Kinoshita, Hj. Matzke, "Polygonization and high burnup structure in nuclear fuels," *Journal of Nuclear Materials,* vol. 247, pp. 108-115, 1997.

[18] Nele Moelans, Bart Blanpain and Patrick Wollants, "An introduction to phase-field modeling of microstructure evolution," *Calphad,* vol. 32, no. 2, pp. 268-294, 2008.

[19] Xian-Ming Baia, Michael R.Tonks, Yongfeng Zhanga and Jason D.Hales, "Multiscale modeling of thermal conductivity of high burnup structures in UO_2 fuels," *Journal of Nuclear Materials,* vol. 470, pp. 208-215, 2016.

[20] Michael R.Tonks, Amani Cheniour and Larry Aagesen, "How to apply the phase field method to model radiation damage," *Computational Materials Science,* vol. 147, pp. 353-362, 2018.

[21] Paul C.Millett, Anter El-Azab, Srujan Rokkam, Michael Tonks and DieterWolf, "Phase-field simulation of irradiated metals: Part I: Void kinetics," *Computational Materials Sciense,* vol. 50, no. 3, pp. 949-959, 2011.

[22] Yulan Li, Shenyang Hu, Xin Sun and Marius Stan, "A review: applications of the phase field method in predicting microstructure and property evolution of irradiated nuclear materials," *npj Computational Materials,* vol. 3, p. 16, 2017.

[23] K. Ahmed , and A. El-Azab, "Phase-field modeling of microstructure evolution in nuclear materials," in *Handbook of Materials Modeling*, Cham, Springer, 2018.

[24] Linyun Liang, Zhi-Gang Mei, Yeon Soo Kim, Bei Ye, Gerard Hofman, Mihai Anitescu and Abdellatif M. Yacout, "Mesoscale model for fission-induced recrystallization in U-7Mo alloy," *Computational Materials Science,* vol. 124, pp. 228-237, 2016.

[25] Linyun Liang, Zhi-Gang Mei and Abdellatif M. Yacout, "Fission-induced recrystallization effect on intergranular bubble-driven swelling in U-Mo fuel," *Computational Materials Science,* vol. 138, pp. 16-26, 2017.

[26] J. Rest, "A model for the influence of microstructure, precipitate pinning and fission gas behavior on irradiation-induced recrystallization of nuclear fuels," *Journal of Nuclear Materials,* vol. 326, pp. 175-184, 2004.

[27] M. Kinoshita, "Towards the mathematical model of rim structure formation," *Journal of Nuclear Materials,* vol. 248, pp. 185-190, 1997.

[28] Wirth, Donghua Xu and Brian, "Spatially Dependent Rate Theory Modeling Of Thermal Desorption Spectrometry Of Helium-Implanted Iron," *Fusion Science and Technology,* vol. 56, pp. 1064-1068, 2009.

[29] Meimei Lia, M.A. Kirkb, P.M. Baldob, Donghua Xuc and B.D. Wirthc, "Study of defect evolution by TEM with in situ ion irradiation and coordinated modeling," *Philosophical Magazine,* vol. 92, pp. 2048-2078, 2012.

[30] Elder, Nikolas Provatas and Ken, Phase-Field Methods in Materials Science and Engineering, Weinheim, Germany: Wiley-VCH, 2010.

[31] Wollants, N. Moelans and B. Blanpain, "Quantitative analysis of grain boundary properties in a generalized phase field model for grain growth in anisotropic systems," *PHYSICAL REVIEW,* vol. 78, no. 2, p. 024113, 2008.

[32] Hongxing Xiao, Chongsheng Long, Hongsheng Chen., "Model for evolution of grain size in the rim region of high burnup UO_2 fuel," *Journal of Nuclear Materials,* vol. 471, pp. 74-79, 2016.

[33] K. Une, K. Nogita, S. Kashibe and M. Imamura., "Microstructural change and its influence on fission gas release in high burnup UO_2 fuel," *Journal of Nuclear Materials,* vol. 188, pp. 65-72, 1992.

[34] D. Frazer, D.Jadernas, N.Bolender, J.Madden, J.Giglio and P.Hosemann, "Elevated temperature microcantilever testing of fresh U-10Mo fuel," *Journal of Nuclear Materials,* vol. 526, p. 151746, 2019.

[35] Khan, Iqra Zubair Awan and Abdul Qadeer, "Recovery, Recrystallization, and Grain-Growth," *GENERAL AND PHYSICAL,* vol. 41, 2019.

[36] Dieter, George E. *Mechanical Metallurgy.* McGraw-Hill Higher Education, 1986.

[37] K. Ahmed, C. A. Yablinsky, A. Schulte, T. Allen and A El-Azab, "Phase field modeling of the effect of porosity on grain growth kinetics in polycrystalline ceramics," vol. 21, p. 23, 2013.

[38] H.S. Zurob, Y. Bre´chet b, and J. Dunlop, "Quantitative criterion for recrystallization nucleation in single-phase alloys: Prediction of critical strains and incubation times," *Acta Materialia,* vol. 54, pp. 3983-3990, 2006.

[39] Turnbul, J. E. Burke, "Recrystallization and grain growth," *Progress in Metal Physics,* vol. 3, pp. 220-244, 1952.

[40] F J Humphreys, and M Hatherly, Recrystallization and related Annealing Phenomena, Oxford: Elsevier Science Ltd., 2004.

[41] Ke Huang, Knut Marthinsen, Qinglong Zhao, Roland E. Logé, "The double-edge effect of second-phase particles on the recrystallization behaviour and associated mechanical properties of metallic materials," *Progress in Materials Science,* vol. 92, pp. 284-359, 2018.

[42] A. N. Kolmogorov, "On The Statistical Theory of Metal Crystallization," *Bulletin of the Academy of Sciences of the USSR,* vol. 1, pp. 355-359, 1937.

[43] E. J. Mittemeijer, Fundamentals of Materials Science, The Microstructure–Property Relationship Using Metals as Model Systems, London: Springer, 2010.

[44] J. Christian, the theory of transformation in metals and alloys, Amestrdam: PERGAMON-Elsavier Science, 2002.

[45] Lusk, Herng-Jeng Jou and Mark, "Comparison of Johnson-Mehl-Avrami-Kologoromov kinetics with a phase-field model for microstructural evolution driven by substructure energy," *PHYSICAL REVIEW,* vol. 55, 1996.

[46] Szpunar, R. D. Doherty and J. A., "Kinetics Of Sub-Grain Coalescence-A Reconsideration Of The Theory," *Acta metall,* vol. 32, no. 10, pp. 1789-1798, 1984.

[47] C. Smith, "Introduction to Grains, Phases, and Interfaces—an Interpretation of Microstructure," *Trans. AIME,* vol. 175, pp. 15-51, 1948.

[48] L. R. Huang K, "Zener Pinning," *Reference Module in Materials Science and Materials Engineering,* 2016.

[49] Karim Ahmed, Michael Tonks, Yongfeng Zhang, Bulent Biner, Anter El-Azab, "Particle-grain boundary interactions: A phase field study," *Computational Materials Science,* vol. 134, pp. 25-37, 2017.

[50] Miracle, K.L. Kendig, "Strengthening mechanisms of an Al-Mg-Sc-Zr alloy," *Acta Materialia,* vol. 50, no. 16, pp. 4165-4175, 2002.

[51] Erhard Hornbogen, Karl-Heinz and Zum Gahr, "Distribution of plastic strain in alloys containing small particles," *Metallography,* vol. 8, no. 3, pp. 181-202, 1975.

[52] Starink, S. C. Wang, "Precipitates and intermetallic phases in precipitation hardening Al–Cu–Mg–(Li) based alloys," *International Materials Reviews,* vol. 50, no. 4, pp. 193-215, 2005.

[53] A. Pineau, A. Benzerga, T. Pardoen, "Failure of metals I: Brittle and ductile fracture," *Acta Materialia,* vol. 107, pp. 421-483, 2016.

[54] Griffith, Alan Arnold, "The phenomena of rupture and flow in solids," *Royal Society,* vol. 221, pp. 582-593, 1921.

[55] David A. Porter, Kenneth E. Easterling, And Mohamed Y. Sherif, Phase Transformations In Metals And Alloys, Third Edition, Broken Sound Parkway Nw: Taylor & Francis Group, Llc, 2009.

[56] J.S.Cheonb, Yeon SooKim G.L.Hofman, "Recrystallization and fission-gas-bubble swelling of U–Mo fuel," *Journal of Nuclear Materials,* vol. 436, pp. 14-22, 2013.

[57] Gwan Yoon Jeong, Yeon Soo Kim and Dong-Seong Sohn, "Mechanical analysis of UMo/Al dispersion fuel," *Journal of Nuclear Materials,* vol. 466, pp. 509-521, 2015.

[58] C.R. Clark, S.L. Hayes M.K. Meyer, G.L. Hofman And J.L Snelgrove, "Update On U-Mo Monolithic And Dispersion Fuel Development," in *8th International Topical Meeting Research Reactor Fuel Management, European Nuclear Society (ENS)*, M ̧nchen, Germany, 2004.

[59] J. Rest, "A model for the effect of the progression ofirradiation-induced recrystallization from initiationto completion on swelling of UO_2 and U–10Mo nuclear fuels," *Journal of Nuclear Materials ,* vol. 346, pp. 226-232, 2005.

[60] Soo, Hofman Gerard L. And Kim Yeon, " A Classification of Uniquely different Types of Nuclear Fission Gas Behavior," *Nuclear Engineering Technology,* vol. 4, pp. 299-308, 2005.

[61] Nele Moelans, Andy Godfrey, Yubin Zhang and Dorte Juul Jensen, "Phase-field simulation study of the migration of recrystallization boundaries," *Physical Review,* vol. 88, 2013.

[62] M. Plapp, "Unified derivation of phase-field models for alloy solidification from a grand-potential functional," *PHYSICAL REVIEW E,* vol. 84, 2011.

[63] N. Moelans, "A quantitative and thermodynamically consistent phase-field interpolation function for multi-phase systems," *Acta Materialia,* vol. 59, no. 3, pp. 1077-1086, 2011.

[64] Larry K. Aagesen, Yipeng Gao, Daniel Schwen and Karim Ahmed, "Grand-potential-based phase-field model for multiple phases, grains, and chemical components," *PHYSICAL REVIEW,* vol. 98, p. 023309, 2018.

[65] Karim Ahmed, Janne Pakarinen, Todd Allenb , and Anter El-Azab, "Phase field simulation of grain growth in porous uranium dioxide," *Journal of Nuclear Materials,* vol. 446, no. 13, pp. 90-99, 2014.

[66] K Ahmed, C A Yablinsky, A Schulte, T Allen and A El-Azab1. 2013, "Phase field modeling of the effect of porosity on grain growth kinetics in polycrystalline ceramics," *Modelling and Simulation in Materials Science and Engineering,* vol. 21, p. 23, 2013.

[67] G. Desai, Pankaj V. Nerikar Karin Rudman Tapan, "Grain Boundaries in Uranium Dioxide: Scanning Electron Microscopy Experiments and Atomistic Simulations," *The American Ceramic Society,* vol. 94, pp. 1893-1900, 2011.

[68] Hj. Matzke, T. Inoue and R.Warren, "The surface energy of UO2 as determined by hertzian indentation," *Journal of Nuclear Materials,* vol. 91, no. 1, pp. 205-220, 1980.

[69] J.B. Ainscough, B.W. Oldfield and J.O. Ware, "Isothermal grain growth kinetics in sintered UO2 pellets," *Journal of Nuclear Materials,* vol. 49, no. 2, pp. 117-128, 1973.

[70] Cody J. Permann, Michael R. Tonks, Bradley Fromm, Derek R. Gaston, "Order parameter re-mapping algorithm for 3D phase field model of grain growth using FEM," *Computational Materials Science,* vol. 115, pp. 18-25, 2016.

[71] Karim Ahmed, Michael Tonks, Yongfeng Zhang, Bulent Biner, Anter El-Azab, "Particle-grain boundary interactions: A phase field study," *Computational Materials Science,* vol. 134, pp. 25-37, 2017.

[72] F. A. Nichols, "Further Comments on the Theory of Grain Growth in Porous Compacts," *Journal of The American Ceramic Society,* vol. 51, pp. 468-469, 1968.

[73] C.H. Hsueh, A.G. Evans and R.L. Coble, "Microstructure development during final/intermediate stage sintering—I. Pore/grain boundary separation," *Acta Metallurgica,* vol. 30, pp. 1269-1279, 1982.

[74] K. Ahmed, Y. Zhang, D. Schwen, C. Permann, and X. Bai, "Model Development in marmout for Hih burn-up structure formation," Idaho National Laboratory, Idaho, 2017.

[75] T. Heo, L. Zhang, Q. Du, and L.Q. Chen, "Incorporating diffuse-interface nuclei in phase-field simulations," *Scripta Materialia,* vol. 63, no. 1, pp. 8-11, 2010.

[76] R. Bullafi, W. Carter and S. Allen, Kinetics of Materials, Cambridge, Massachusetts, USA: Wiley, 2005.

[77] Tonks, Larry K. Aagesen Daniel Schwen Karim Ahmed and Michael, "Quantifying elastic energy effects on interfacial energy in the Kim-Kim-Suzuki phase-field model with different interpolation schemes," *Computational Materials Science,* vol. 140, pp. 10-21, 2017.

[78] R.D. Doherty, D.A. Hughes, F.J. Humphreys, J.J. Jonas, D. Juul Jensen, M.E. Kassner, "Current issues in recrystallization: a review," *Materials Science and Engineering,* vol. A238, pp. 219-274, 1997.

[79] F. H. a. M. Hatherly, Recrystallization and Related Annealing Phenomena, Kidlingtom, Oxford, UK: Elsevier, 2004.

[80] Technology, National Institute of Standards, "Elastic Moduli Data for Polycrystalline Ceramics," 2002. [Online]. Available: https://srdata.nist.gov/CeramicDataPortal/Elasticity/UO2. [Accessed August 2019].

[81] R.D. Doherty, D.A. Hughes, F.J. Humphreys, J.J. Jonas, D. Juul Jensen, "Current issues in recrystallization: a review," *Materials Science and Engineering,* vol. 238, pp. 219-279, 1997.

[82] Rodrigo Pinto De Siqueira, Hugo Ricardo Zschommler Sandim, And Dierk Raabe, "Particle Stimulated Nucleation in Coarse-Grained Ferritic Stainless Steel," *Metallurgical and Materials Transactions A,* vol. 44, no. 1, pp. 469-478, 2013.

[83] J. Rest, "A model for the effect of the progression of irradiation-induced recrystallization from initiation to completion on swelling of UO2 and U–10Mo nuclear fuels," vol. 346, pp. 226-232, 2005.

[84] Soo, Hofman Gerard L. And Kim Yeon, "A classification of uniquely different types of nuclear fission gas behavior," *Nuclear Engineering and Technology,* vol. 37, pp. 299-308, 2005.